AGU ADVANCING EARTH AND SPACE SCIENCE

Water Resources Research

RESEARCH ARTICLE
10.1029/2020WR029343

Horton Index: Conceptual Framework for Exploring Multi-Scale Links Between Catchment Water Balance and Vegetation Dynamics

Guta Wakbulcho Abeshu[1] **and Hong-Yi Li**[1]

[1]Department of Civil and Environmental Engineering, University of Houston, Houston, TX, USA

Key Points:

- Derivation and validation of an analytical framework of Horton Index applicable over long-term, annual, and monthly scales across biomes
- Vegetation regulates catchment storage partitioning into vaporization and baseflow, then vaporization into initial and continuing components
- Emergent space-time similarity patterns detected empirically and explained theoretically using the analytical framework

Correspondence to:
H.-Y. Li,
hongyili.jadison@gmail.com

Citation:
Abeshu, G. W., & Li, H.-Y. (2021). Horton Index: Conceptual framework for exploring multi-scale links between catchment water balance and vegetation dynamics. *Water Resources Research*, *57*, e2020WR029343. https://doi.org/10.1029/2020WR029343

Received 27 NOV 2020
Accepted 7 MAY 2021

Abstract This paper is motivated to understand the multi-temporal scale characteristics of Horton Index (HI), an indicator of catchment-scale plant water use defined as the ratio of catchment vaporization (total evapotranspiration) to catchment wetting (precipitation minus surface runoff). Based on the generalized proportionality hypothesis, we first develop an analytical framework of HI applicable at multi-temporal scales as a single function of ecological aridity index (EAI), defined as the ratio of potential evapotranspiration to catchment wetting. We successfully validate this framework at the long-term, annual, and monthly scales at 343 natural catchments over the conterminous United States under varying climate and vegetation regimes. We show that vegetation plays an important role in regulating not only the partitioning of catchment wetting into vertical vaporization and horizontal baseflow, but also further partitioning of vaporization into initial and continuing components. Aided by this framework, we reveal emergent space-time similarity patterns between HI's spatial (inter-catchment, regional) and temporal (within-catchment, inter and intra-annual) variability. On the one hand, HI increases with EAI, both spatially and temporally, following similar trends predicted by the analytical framework. On the other hand, the slopes of HI ~ EAI relationships, denoted as d (HI)/d (EAI), decreased with EAI both spatially and temporally and, again, following similar trends suggested by the analytical framework. These findings suggest the promising potential of Horton Index as a conceptual yet quantitative framework for improving understanding and modeling of multi-scale ecological and hydrological processes and their interactions.

1. Introduction

Horton Index, a dimensionless ratio of catchment vaporization (total evapotranspiration) to wetting (the portion of precipitation that wets canopy, ground surface, and soil), has been a valuable signature to reveal the links between catchment water balance and vegetation dynamics (Brooks et al., 2011; Horton, 1933; Sivapalan et al., 2011; Tang & Wang, 2017; Troch et al., 2009; Voepel et al., 2011). Horton (1933) found the HI calculated over the growing period (May to October) at a pristine catchment show a remarkable constancy between years despite substantial inter-annual precipitation variability. He postulated that the reason for this constancy might be that vegetation maximizes productivity relative to available water, echoing back to the concept of maximum possible actual evapotranspiration (Ol'dekop, 1911). Based on his hydrologic partitioning theory, L'vovich (1979) also confirmed a maximum attainable actual evapotranspiration for a given soil wetting magnitude, hence recognizing the role of soil-vegetation interactions in hydrologic partitioning.

It was not until decades later that Troch et al. (2009) revisited HI and its between-year constancy using 89 catchments distributed across different ecoregions. Using this index, Troch et al. (2009) revealed a space-time symmetry between the inter-catchment and inter-year variability of HI, which they suggested might be underpinned by a similarity across biomes in short- and long-term adaptation strategies of vegetation to climate variability.

Inspired by Troch et al. (2009), there have been many data-driven studies evaluating the impacts of climate, soil, and topographic conditions on HI variations over the past decade. For example, Voepel et al. (2011) found that climate conditions exerted a first-order control on the HI variations, for example, there was a power-law relationship between HI and Aridity Index; whilst topographic characteristics such as topographic slope and mean elevation only exerted a secondary control. Using 86 of the 89 catchments utilized by Troch et al. (2009), Rasmussen (2012) related the HI to effective energy and mass transfer (EEMT). Here, the EEMT represents energy that can perform work on the subsurface and has two components, the

energy flux associated with effective precipitation and the energy flux from net primary production. The result showed a strong negative correlation between EEMT and HI, indicating that water-limited catchments correspond to lower EEMT. Zapata-Rios et al. (2016) examined HI characteristics over high-elevation catchments. They reported that snowpack conditions explained over 95% of the HI variability and that, in turn, influenced annual vegetation greening. They also found that the topographic aspect did influence the magnitude of HI but only during wet years.

Moreover, HI has been used as a valuable diagnostic signature for catchment water balance under the influences of climate, soil, and biomes. Guardiola-Claramonte et al. (2010) used annual HI as one of the objective functions to calibrate and validate their catchment water balance simulations. Brooks et al. (2011) and Voepel et al. (2011) showed that HI could be a good predictor of inter-annual changes in vegetation cover and greenness. Harman et al. (2011) derived analytical expressions that relate the flow elasticities to long-term mean HI. Thompson et al. (2011) showed the scale-dependence of catchment water balance partitioning on a hierarchical flow path network with a scale-dependent expression of HI. Wang and Tang (2014) and Tang and Wang (2017) parameterized their Budyko-type models directly or indirectly with HI. Arciniega-Esparza et al. (2017) and Troch et al. (2018) found that HI was a highly efficient predictor of the spatial variability of average maximum deep storage, low-flows, and groundwater recharge in ungauged catchments with different types of climate, soils, geology, and vegetation cover.

The aforementioned HI-related studies are nevertheless mostly data-driven, that is, without providing a mechanistic, generalizable understanding across space and time. The only exceptions are Sivapalan et al. (2011) and Schaefli et al. (2012). Sivapalan et al. (2011) derived a functional formula of HI as a function of two dimensionless similarity variables (rescaled annual precipitation and aridity index) based on the two-stage hydrologic partitioning theory (L'vovich, 1979; Ponce & Shetty, 1995a, 1995b). They then revealed a space-time symmetry of inter-catchment (regional) and inter-annual variability of HI Schaefli et al. (2012) derived an analytical expression for HI as a function of available storage in the atmospheric column and a constant k (the ratio of maximum potential evaporation to maximum runoff). They confirmed the power-law relationship between HI and AI as suggested by Voepel et al. (2011).

However, neither Sivapalan et al. (2011) or Schaefli et al. (2012) examined HI's intra-annual variability. In fact, most of the data-driven HI-related studies have also focused on the annual scale by neglecting soil moisture storage change. As such, the importance of intra-annual variability of HI has nevertheless not been fully explored, particularly over the growing season (Horton, 1933; Troch et al., 2009). There is substantial seasonal variability in the dynamics of most vegetation types. For example, in the U.S., for most vegetation types, a calendar year can be divided into a growing season and a dormant season (Kukal & Irmak, 2018). Vegetation typically acquires and consumes much more water via transpiration during the growing season than the dormant season (Schlesinger & Jasechko, 2014; Wang et al., 2014; Zhou et al., 2016). It is thus necessary to incorporate intra-annual variability for improving the understanding of HI variability and the role of vegetation that cannot be effectively captured at the annual scale (Sivapalan et al., 2011; Troch et al., 2009).

The mathematical derivation of Sivapalan et al. (2011) was directly based on the two-stage hydrologic partitioning theory pioneered by L'vovich (1979) and later on theoretically proven by Ponce and Shetty (1995a, 1995b). The two-stage hydrologic partitioning theory quantifies the partitioning of precipitation into fast flow and wetting (1st-stage) and then partitioning of wetting into baseflow and vaporization (2nd-stage). The 2nd-stage partitioning is directly relevant to HI. Ponce and Shetty (1995a, 1995b) provided the theoretical foundation of this hydrologic partitioning theory by generalizing the Proportionality Hypothesis underpinning the Soil Conservation Service Curve Number (SCS-CN) method (SCS, 1985). Given that Z is a certain amount of water that can be portioned into X and Y (e.g., precipitation portioned into soil retention and excess runoff, or catchment wetting partitioned into vaporization and baseflow), the Generalized Proportionality Hypothesis (GPH) states that

$$\frac{X - X_0}{X_p - X_0} = \frac{Y}{Z - X_0} \tag{1}$$

Here X_p is the potential of X, and X_o is the initial fraction of X (e.g., initial soil abstraction or initial vaporization).

Ponce and Shetty (1995a, 1995b) showed that GPH could be used to theoretically derive the functional formulas for both stages of the two-stage hydrologic partitioning. For the 2nd-stage partitioning, applying GPH leads to

$$\frac{E - E_0}{E_p - E_0} = \frac{Q_b}{W - E_0} \tag{2}$$

where E is total vaporization. E_0 is initial vaporization. E_p is potential vaporization. Q_b is baseflow. W is total wetting. Note that Equation 2 is for long-term catchment water balance, hence storage change is neglected (Sivapalan et al., 2011; Tang & Wang, 2017; Wang et al., 2015).

Interestingly, Wang and Tang (2014) showed that GPH could also be used to theoretically derive the Budyko-type formula. A Budyko-type formula is essentially quantifying a one-stage hydrologic partitioning, that is, total precipitation partitioned into total runoff (include fast flow and baseflow) and vaporization. By applying GPH to this one-stage partitioning, Wang and Tang (2014) derived a generic, one-parameter expression of the Budyko model for long-term catchment water balance and suggested that the original deterministic Budyko curve (Budyko, 1974) and Fu's equation (Fu, 1981) are just two specific forms of this generic expression.

More importantly, Wang et al. (2015) later proved that GPH could be theoretically derived from the thermodynamic principle, that is, Maximum Entropy Production. In particular, they showed that the 2nd-stage partitioning at the long-term scale could directly result from the Maximum Entropy Production principle. Wang (2018) was then able to theoretically derive the proportionality relationship used in the SCS-CN method following a different route than the Maximum Entropy Production principle, that is, by proposing a new probability density function for the spatial distribution of soil water storage capacity. Hooshyar and Wang (2016) also demonstrated the physical basis of the SCS-CN proportionality hypothesis by deriving it from Richard's equation but for relatively specific conditions, that is, coarse-textured soil, shallow water table, and an early stage of ponded infiltration.

So far, GPH has been validated empirically (SCS, 1985), indirectly by Ponce and Shetty (1995a, 1995b) and Wang and Tang (2014), and theoretically by Wang et al. (2015), Hooshyar and Wang (2016) and Wang (2018). It appears to be a very powerful theoretical framework not only underpinning now well accepted two-stage hydrologic partitioning theory and Budyko hypothesis, but also facilitating new hydrologic theoretical explorations.

Our objectives are therefore three-fold: (a) Developing a new analytical framework of HI applicable at multi-temporal scales based on the Generalized Proportionality Hypothesis; (b) Validating the analytical framework over a large number of catchments with various climate, vegetation, soil and topographic conditions with a main focus on the monthly scale; and (c) Using the new analytical framework to help understand the mechanisms underpinning the emergent patterns of HI's inter- and intra-annual variability. The rest of this paper is organized as follows: Section 2 introduces the analytical framework. Section 3 describes the validation of it at both annual and monthly scales. Section 4 presents the emergent patterns in the HI's spatial (inter-catchment) variability and temporal (inter- and intra-annual) variability, and interprets them using the analytical framework. Section 5 closes with a summary and further discussion.

2. Analytical Framework of Horton Index

2.1. General Horton Index Definition

So far, at annual and long-term scales, HI has been mostly defined and used as the ratio of catchment vaporization to catchment wetting (Horton, 1933; Troch et al., 2009), without accounting for effects of storage carryover between-years. Troch et al. (2009) suggested accounting for storage carryover from winter into spring for using HI. For multi-scale applicability, we thus adopt a general definition of HI as following:

$$HI = \frac{E}{W - \Delta S} \tag{3}$$

where E is catchment vaporization (or actual evapotranspiration), $W - \Delta S$ is catchment wetting accounting for the storage change. We hereafter consider $(W - \Delta S)$ as effective catchment wetting, which is the amount of water available for vaporization and baseflow at any time scales. Effective catchment wetting can also be viewed as the maximum water supply for vegetation use. The definition in Equation 3 can thus be applied at any time scales. In this study, we define and examine HI at the long-term, annual, and monthly scales. For the long-term scale, HI is defined as the ratio of long-term average evapotranspiration to long-term average catchment wetting and denoted as *long-term HI* hereinafter. For the annual scale, HI is defined as the ratio of annual total evapotranspiration to annual effective catchment wetting for any specific calendar year and denoted as *annual HI*. For the monthly scale, HI is defined as the ratio of monthly total evapotranspiration over monthly effective catchment wetting for any month and denoted as *monthly HI*.

2.2. Mathematical Derivations

At the catchment scale, total liquid precipitation (rainfall + snowmelt), P, can be partitioned into total surface runoff (Q_s) and catchment wetting (W), which includes total infiltration and interception by vegetation canopy and surface depressions (see Figure 1a):

$$P = Q_s + W \tag{4}$$

Catchment wetting occurs in two phases: Initial wetting (W_o) due to interception by vegetation and ground surface depressions, and continuing wetting (W_c) due to soil infiltration. Catchment wetting can then be further partitioned into catchment vaporization (E), base flow (Q_b), and soil water storage change (ΔS) (see Figure 1b):

$$W = E + Q_b + \Delta S \tag{5}$$

We now apply GPH to the 2nd-stage partitioning at the monthly scale:

$$\frac{E - E_o}{E_p - E_o} = \frac{Q_b}{W - \Delta S - E_o} \tag{6}$$

E_0 is the portion of vaporization that occurs at the initial stage, that is, evaporation from canopy interception and surface depression ponding and transpiration from shallow water storage (mostly in the unsaturated zone). Note that with Equation 6 here we are only assuming that GPH is valid for the 2nd-stage partitioning at the monthly scale. Whether it is valid at finer time scales is beyond the scope of this study.

Rearranging (6) for Q_b, we obtain

$$\frac{Q_b}{W - \Delta S} = \frac{\left(\frac{E}{W - \Delta S} - \frac{E_o}{W - \Delta S}\right)\left(1 - \frac{E_o}{W - \Delta S}\right)}{\frac{E_p}{W - \Delta S} - \frac{E_o}{W - \Delta S}} \tag{7}$$

Similar to the SCS-CN method (SCS, 1985), Ponce and Shetty (1995a, 1995b) and Wang and Tang (2014), we consider the whole vaporization process occurs at two stages: An initial stage followed by a continuing stage.

$$E = E_0 + E_c \tag{8a}$$

$$E_0 = \lambda E \tag{8b}$$

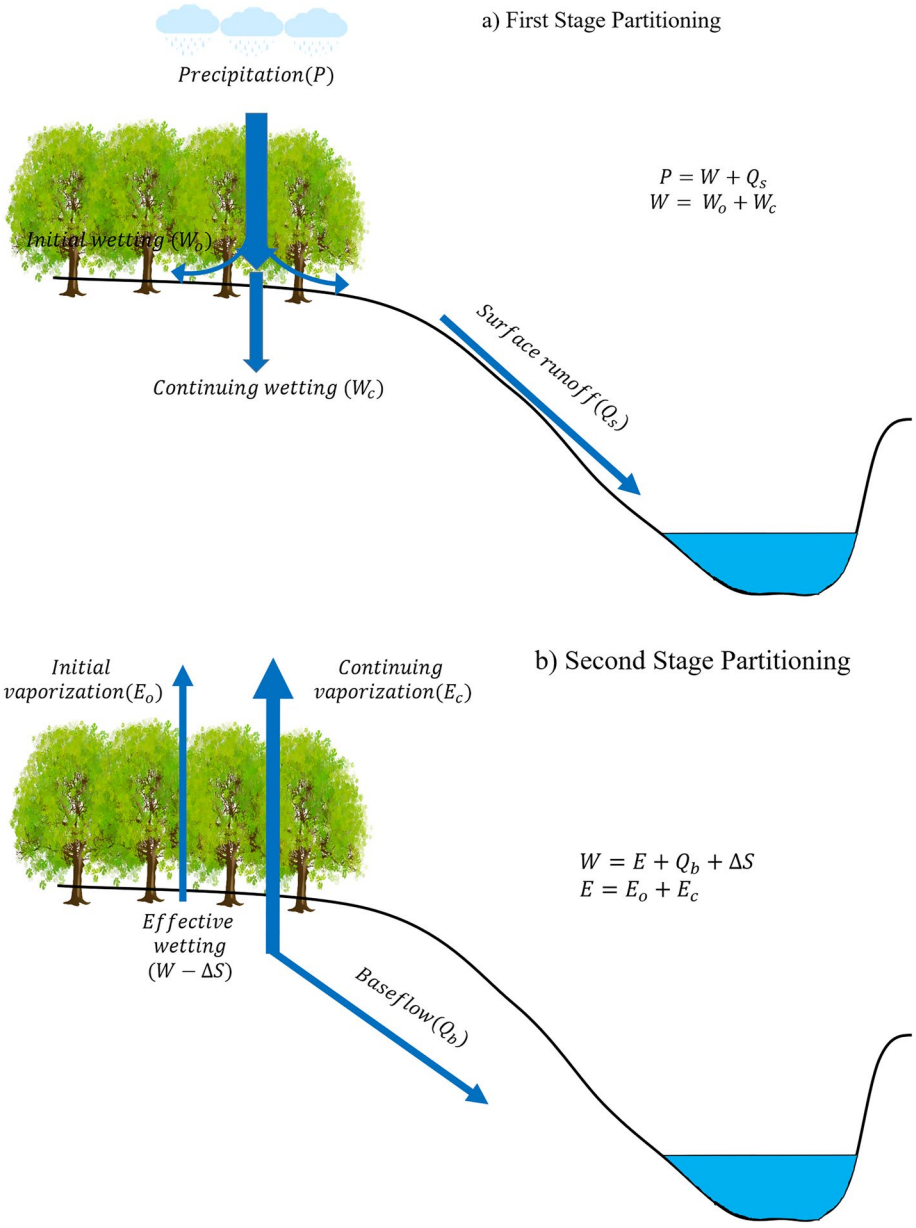

Figure 1. Conceptual-level two-stage hydrologic partitioning scheme, (a) First-Stage Partitioning for effective precipitation partitioning and (b) Second-Stage Partitioning for effective catchment wetness partitioning.

E_c is the portion of vaporization that occurs after the initial stage, mostly transpiration from deeper soil water storage that is very close to or below the groundwater table. λ is a dimensionless fraction parameter. We provide a more detailed discussion on E_0 and λ later in Section 3.

From Equations 7 and 8, we get

$$\frac{Q_b}{W-\Delta S} = \frac{(1-\lambda)\frac{E}{W-\Delta S} - (\lambda-\lambda^2)\left(\frac{E}{W-\Delta S}\right)^2}{\frac{E_p}{W-\Delta S} - \lambda\frac{E}{W-\Delta S}} \tag{9}$$

From Equations 5 and 9, we get

$$\left(2\lambda-\lambda^2\right)\left(\frac{E}{W-\Delta S}\right)^2-\left(1+\frac{E_p}{W-\Delta S}\right)\left(\frac{E}{W-\Delta S}\right)+\frac{E_p}{W-\Delta S}=0 \tag{10}$$

When $\lambda = 0$, Equation 10 gives

$$\frac{E}{W-\Delta S}=\frac{\frac{E_p}{W-\Delta S}}{1+\frac{E_p}{W-\Delta S}} \tag{11}$$

When $\lambda > 0$, Equation 10 is a typical quadratic equation for $\left(E/\left(W-\Delta S\right)\right)$, solving it yields

$$\frac{E}{W-\Delta S}=\frac{\left(1+\frac{E_p}{W-\Delta S}\right)\pm\sqrt{\left(1+\frac{E_p}{W-\Delta S}\right)^2-4\left(2\lambda-\lambda^2\right)\frac{E_p}{W-\Delta S}}}{2\left(2\lambda-\lambda^2\right)} \tag{12}$$

If taking the plus sign in Equation 12, one will always obtain $\frac{E}{W-\Delta S}\geq 1.0$, while $\frac{E}{W-\Delta S}$ should always be no larger than 1.0 (Equation 5). So in Equation 12 we take the minus sign and obtain the following equation:

$$HI=\frac{E}{W-\Delta S}=\frac{1}{2\left(2\lambda-\lambda^2\right)}\left\{\left(1+\frac{E_p}{W-\Delta S}\right)-\left[1+\left(2-8\lambda+4\lambda^2\right)\frac{E_p}{W-\Delta S}+\left(\frac{E_p}{W-\Delta S}\right)^2\right]^{0.5}\right\} \tag{13}$$

Equation 13 is thus an analytic expression of HI, which applies to the long-term, annual, and monthly scales.

Hereafter we refer to the ratio of potential evapotranspiration to effective catchment wetness as ecological aridity index (EAI), which quantifies the interaction between energy supply and water supply for plant water use at the catchment scale. Note for convenience, we define EAI at the long-term, annual, and monthly time scales similarly to HI, and hereinafter denote them as long-term, annual, and monthly EAI, respectively. Compared to the well-known aridity index (AI), defined as the ratio of potential evapotranspiration to total precipitation, EAI is overall larger since it excludes surface runoff from water supply for vaporization. Intuitively it is more physically meaningful from the plant water use point of view since surface runoff will rarely be available for vaporization in the real world. Figure 2a provides a conceptual diagram of Equation 13, which includes a theoretical upper-bound of HI when $\lambda = 1.0$ (solid blue line), and theoretical lower-bound when $\lambda = 0$ (dashed blue line). When $EAI < 1.0$, the water supply for vaporization is larger than the evaporative energy demand, and the catchment is in an energy-limited or ecologically wet state. When $EAI > 1.0$, the water supply for vaporization is less than the energy supply, and the catchment is in a water-limited or ecologically dry state.

One can also see that the changing rate of HI is gradually decreasing with EAI, suggesting that HI variability might be decreasing when a catchment is moving from an ecologically wetter state to an ecologically drier state. To quantify the changing rate of HI with EAI, we take the derivative of Equation 13, and obtain

$$\frac{d\left(HI\right)}{d\left(EAI\right)}=\frac{1}{2\left(2\lambda-\lambda^2\right)}\left\{1-\left(1-4\lambda+2\lambda^2+\frac{E_p}{W-\Delta S}\right)\left[1+\left(2-8\lambda+4\lambda^2\right)\frac{E_p}{W-\Delta S}+\left(\frac{E_p}{W-\Delta S}\right)^2\right]^{-0.5}\right\} \tag{14}$$

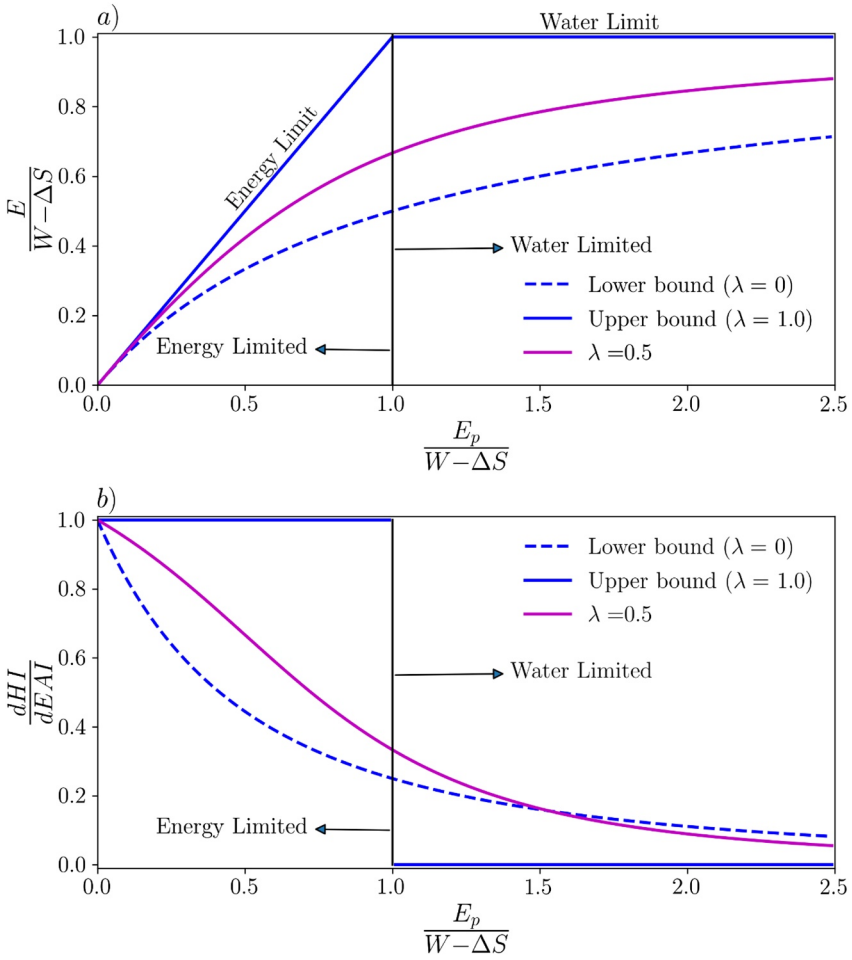

Figure 2. a) Theoretical bounds of the new Horton Index functional framework (Equation 13). The model parameter, λ, which is defined as the ratio of initial vaporization to total vaporization, varies between 0 and 1. The function produces the upper bound (energy and water limit lines) at $\lambda = 1$ and the lower bound at $\lambda = 0$. Like the traditional Budyko curve, based on the potential energy and water available for vaporization, the function space can also be classified into two as energy limited ($E_p < W - \Delta S$) and water limited ($E_p > W - \Delta S$). b) Theoretical bounds of the changing rate of HI with EAI (Equation 14).

This $d(HI) / d(EAI)$ is thus capturing the gradually decreasing slope of the HI ~ EAI curve, as shown in Figure 2b. $d(HI) / d(EAI)$ is overall more than 0.3 when a catchment is ecologically humid, that is, $EAI < 1.0$, suggesting relatively large variability of HI between humid catchments (spatial variability) or humid years (temporal variability). When a catchment is ecologically dry, that is, $EAI > 1.0$, $d(HI) / d(EAI)$ drops quickly and is mostly below 0.1 when $EAI > 2.0$, suggesting that HI remains constant among dry catchments (spatial variability) or dry years (temporal variability). This small spatiotemporal variability of HI is consistent with the previous empirical findings that HI is relatively constant in dry years or arid catchments (Horton, 1933; Troch et al., 2009).

3. Validation of the Analytical Framework

3.1. CAMELS Data Set

The data used in this study are mainly from the Catchment Attributes and MEteorology for Large-sample Studies (CAMELS) data set (Addor et al., 2017; Newman et al., 2015). CAMELS includes 671 small to medium-sized nearly pristine catchments distributed across biomes, climatic, and topographic gradients of the contiguous United States. CAMELS provides observed daily precipitation, streamflow, and maximum and

minimum temperature data for each catchment in 1980–2014. It also offers topographic, soil, and vegetation attributes such as elevation, mean topographic slope, soil hydraulic conductivity, soil depth, porosity, dominant vegetation cover, monthly leaf area index (LAI), root depth, etc., Besides the observed data, CAMELS also provides model simulated hydrologic variables such as actual and potential evapotranspiration, a by-product of streamflow simulation using the coupled Snow-17 and SAC-SMA models, which have been validated against the observed streamflow data (Addor et al., 2017).

For analysis purposes, we perform the following filtering and post-processing steps of CAMELS data.

(1) In some CAMELS catchments, there are missing records in the observed streamflow data. We exclude those catchments without complete daily streamflow records in 1982–2012
(2) Model simulated evapotranspiration data from CAMELS is an essential part of our analysis, but there has been uncertainty (Newman et al., 2015). To minimize the impacts of modeling uncertainty, we adapt a criterion expressed as $\left|\bar{E}_{obs} - \bar{E}_{sim}\right| < 10\% * \bar{E}_{obs}$. Here $\bar{E}_{sim}$ is the long-term average of simulated evapotranspiration in 1982–2012. $\bar{E}_{obs}$ is calculated as the long-term average of observed precipitation subtract the long-term average of observed streamflow. We exclude those catchments that do not satisfy this criterion
(3) Within the CAMELS vegetation attributes, each catchment's dominant vegetation type is available along with the percentage of catchment area it covers. For the entire data set, the dominant cover fraction percentage ranges from 31.45% to 100%. Here, we consider a specific vegetation cover as the dominant vegetation cover if it takes more than 50% of the total catchment area. Thus, we further exclude those catchments without any vegetation cover taking more than 50% of the catchment areas, that is, no dominant vegetation cover
(4) We select 343 CAMELS catchments after Steps 1∼3. The CAMELS catchments belong to 11 different dominant vegetation cover types, as shown in Figure 3a. For convenience, we further group them into six vegetation cover types: Croplands and Croplands/Natural vegetation mosaic (denoted as *CL/NVM*, 99 catchments), Deciduous Broadleaf (denoted as *DBF*, 82 catchments), Evergreen Needleleaf and Broadleaf Forest (denoted as *EF*, 22 catchments), Mixed Forests (denoted as *MF*, 50 catchments), Grasslands (denoted as *GL*, 40 catchments) and Savannas, Woody Savannas and Open/Closed Shrublands (denoted as *WS* + *SL*, 50 catchments). Figure 3b shows that most forested catchments (DBF, EF and MF) are located in the humid or semi-humid climate regions, as indicated by the aridity index (AI, here defined as the ratio of long-term average potential evapotranspiration over precipitation) values less than 1.0. Those non-forested catchments (CL/NVM, GL and WS + SL) are located in the arid or semi-arid climate regions
(5) Note that in this study, the final precipitation data employed are essentially daily rainfall + snowmelt time series, which are directly taken from the CAMELS data set
(6) At each selected catchment, the observed daily streamflow time series is separated into daily surface runoff and daily baseflow time series using the one-parameter recursive digital filtering method (Nathan & McMahon, 1990)

3.2. Validating the Analytical Framework Over the CAMELS Catchments

To evaluate the analytical framework, we first estimate the monthly HI time series at each catchment directly using the CAMELS data. E is taken from the CAMELS simulated daily evapotranspiration time series. $W - \Delta S$ is calculated indirectly as $E + Q_b$, according to Equation 5. We hereafter denote those HI values calculated using the CAMELS data set as "estimated" for easy reading, and those derived using the analytical framework as "analytical." For evaluating the closeness between the "estimated" and "analytical" HI series, we use the Kling-Gupta Efficiency (KGE) (Gupta et al., 2009) and Normalized Root Mean Square Error (NRMSE). Overall, the higher the KGE value, the closer the "estimated" and "analytical" HI series, and KGE = 1.0 means a perfect match. Similarly, the smaller the NRMSE, the closer the "estimated" and "analytical" HI series and NRMSE = 0.0 means a perfect match. At each catchment, we calibrate the λ value at the monthly scale in the calibration period 1982–2001 to reach the best match between the "estimated" and "analytical" monthly HI time series, as indicated by the optimal KGE value. The optimal KGE values are no less than 0.5 and 0.8 for over 95% and 87% of the 343 catchments, respectively (as shown in Figures 4a and 4b), suggesting the promising predicting power of the analytical framework. The resulted λ values from

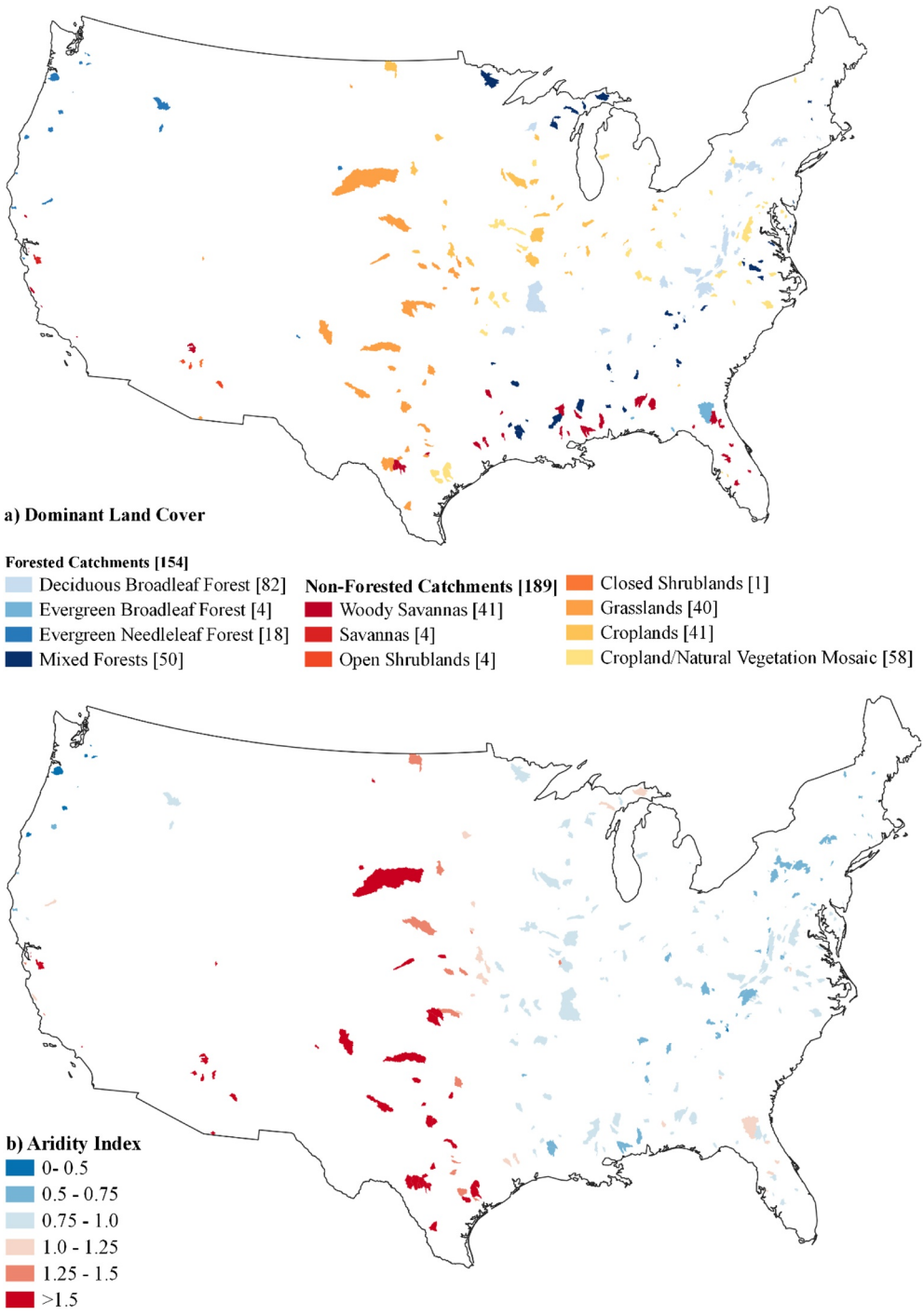

Figure 3. Selected 343 CAMELS catchments: (a) Dominant biomes, (b) Aridity Index (E_p/P).

this calibration process are hereinafter denoted as the "calibrated." We then apply the calibrated λ value corresponding to each catchment in the validation period 2002–2012, 90% and 82% of the catchments have the KGE values no less than 0.5 and 0.8, respectively, indicating the representativeness of the calibrated λ values over the whole study period 1982–2012. The NRMSE values between the "estimated" and "analytical" HI monthly time series are mostly less than 0.1 in both the calibration and validation periods (as shown in Figures 4c and 4d), again indicating good prediction power of the analytical framework. Note that since the normalizing factor (i.e., long-term HI) is always ≤1, NRMSE ≥ RMSE.

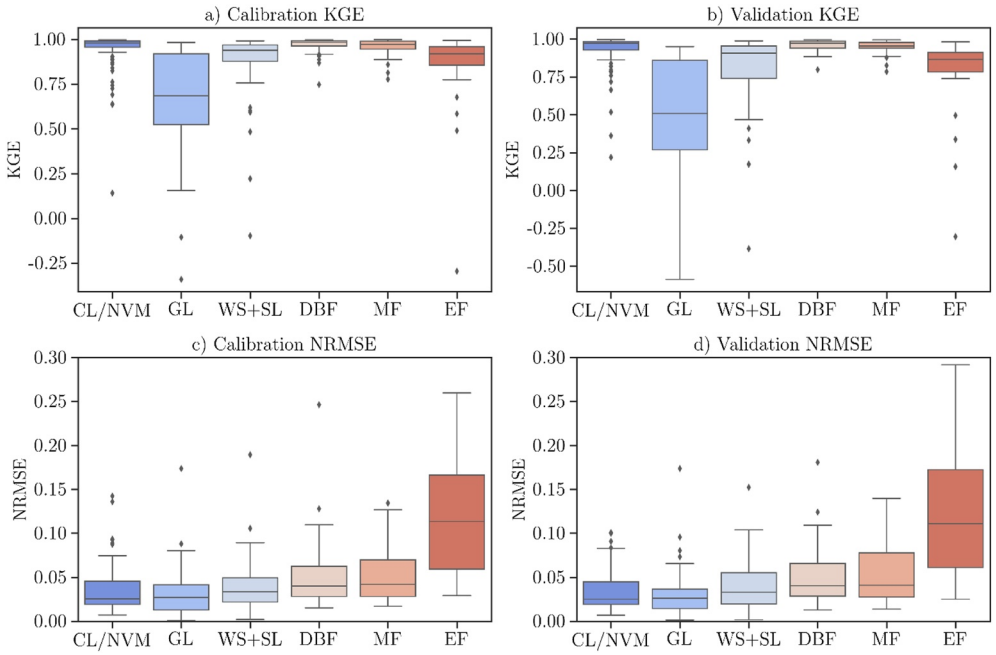

Figure 4. Performance of the analytical formula. Box-plots of; (a). KGE values for different vegetation types in the calibration period (1982–2001); (b). KGE values in the validation period (2002–2012); (c). NRMSE values in the calibration period; (d). NRMSE values in the validation period. CV/NVM: Croplands and Croplands/Natural vegetation mosaic; DBF: Deciduous Broadleaf; EF: Evergreen Needleleaf and Broadleaf Forest; MF: Mixed Forests; GL: Grasslands; WS + SL: Savannas, Woody Savannas and Open/Closed Shrublands.

Regarding specific vegetation types, the analytical framework performs very well at the CL/NVM, MF, DBF, and WS + SL dominated catchments, but only reasonably well at the GL (according to KGE) and EF (according to NRMSE) dominated catchments. By looking into the details of those individual catchments where the analytical framework does not perform well, we find that poor KGE results are partially related to the weak seasonal variability of estimated HI. We use the coefficient of variation (CV, the ratio of the standard deviation to mean) to compute the variability of the estimated HI. In total, only 39 catchments have KGE values less than 0.75, of which 34 have the CV values less than 10%. Visual inspection of these catchments shows that the low KGE values do not necessarily imply model incapability. Instead, since the estimated HI index is slightly invariable, the framework's small overestimation/underestimation is somehow exaggerated by the KGE metric, which is evident by the NRMSE box-plots in Figures 4c and 4d, that is, the NRMSE values are mostly less than 0.1, except for the EF dominant catchments.

To illustrate more detailed HI variations at individual catchments, we select two representative catchments out of each of the six biome regimes, that is, CL/NVM, DBF, EF, MF, GL, and WS + SL, based on Figure 4. Within each biome regime, there are a number of catchments under various climate conditions, that is, a range of AI values. For each biome regime, we select one catchment with relatively higher AI value, and another with relatively lower AI values. Figure 5 shows the "estimated" (blue lines) and "analytical" (red lines) monthly HI time series at the representative catchments. Each row is for one biome. The left column is for the catchments with relatively higher AI values. Overall, the analytical framework reproduces the monthly HI time series quite well in most catchments.

There are nevertheless noticeable biases in the peak HI values, for example, at the EF and GL catchments, as indicated by the relatively low KGE values (for the GL dominant catchments) and high NRMSE values (for the EF dominant catchments). There are several possible reasons for the biases: (a) The NRMSE values for the EF dominant catchments are slightly higher than others' primarily because of the model's slight overestimation of seasonal peak values for this type of catchments. During most of the year, these catchments are in an energy-limited state. However, most of them become water-limited during a couple of growing-season months with peak HI values. The slight overestimation of the peak value possibly arises

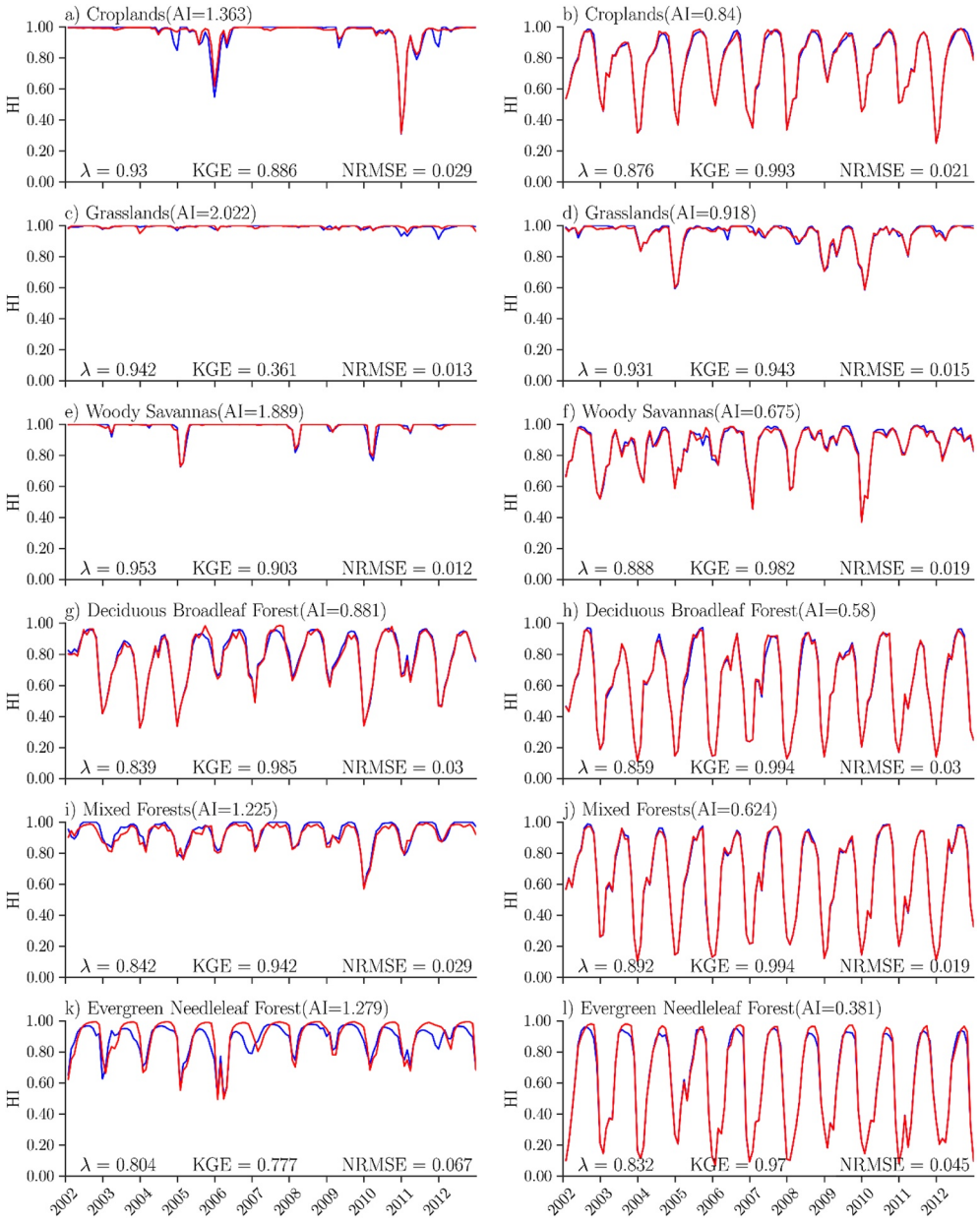

Figure 5. Horton Index monthly time series over the analytical framework validation period (2002–2012) for selected catchments. The blue and red lines are for the estimated and analytical HI time series, respectively. The corresponding USGS gage ID for the catchments are, (a) 5123400, (b) 3241500, (c) 6447000, (d) 6917000, (e) 9505350, (f) 2481000, (g) 3173000, (h) 1413500, (i) 2212600, (j) 1162500, (k) 11162500, and (l) 14325000.

from a failure to capture transition into and out of this short period since the calibration is dominated by those months in an energy-limited state with relatively lower HI values. (b) Temperature and precipitation (magnitude, frequency, and timing) exert strong controls on grassland ecosystems' productivity and water-use (Hufkens et al., 2016). Hence, growth and productivity are highly dynamic even at a sub-monthly temporal scale, that is, weekly or daily, and this sub-monthly variation may have led to strong inter-annual variability of growth and productivity (Hufkens et al., 2016). Therefore, the biases of monthly HI estimation in the GL dominant catchments are likely because that the analytical framework is not well capturing the sub-monthly timescale characteristics, which is an important factor in the strong inter-year variability of grassland dormant-season water-use.

Despite the biases, Figure 5 shows that the analytical framework is reproducing the HI seasonal variations quite well across biomes. In each catchment, the drier months can be further grouped into a growing season (on average May to October for the contiguous United States) when plan transpiration is high. The wetter months can be grouped into a dormant season (November to April) when plant transpiration is much less. HI's seasonal variation is stronger at those catchments under more humid climates, that is, lower AI values. Particularly, during the dormant season (including late fall, winter and early spring), the monthly HI values in the relatively humid catchments are significantly lower than those relatively arid catchments. This difference can be attributed to the different climatic conditions (see Figure 3). Most forested catchments are located in the relatively humid climate regions, where the water supply for vaporization (precipitation) is overall no less than the evaporative energy demand (potential evapotranspiration). In fact, in these forested catchments, the monthly total vaporization (E) is mostly less than the monthly catchment wetness ($W - \Delta S$). In the dormant season, at the forested catchments, the total vaporization is small owing to minimum evaporative energy demand, and the catchment wetness remains a fair amount; while at the non-forested catchments, the total vaporization is at the similar level as those forested catchments, but the catchment wetness is small since it has been depleted by relatively larger vaporization in the growing season.

The difference in the monthly HI values among the catchments can also be attributed to different vegetation phenology among various biomes. In most forested catchments, usually, there is a dense understory and a litter layer, which help reduce soil evaporation during the dormant season by blocking soil moisture from the atmosphere, hence not only reducing vaporization and surface runoff but also increasing catchment wetness (Gomyo & Kuraji, 2016; Sakaguchi & Zeng, 2009; Song et al., 1997). In the broadleaf forests, most leaves fall off in the dormant season leading to not only a thicker litter layer but also significantly reduced transpiration from leaves. In the evergreen forests, the leaves largely remain on the trees even during the dormant season, but the trees lower their carbon utilization rate (i.e., downregulation of photosynthetic capacity) in response to the low-temperature conditions (Adams et al., 2004; Öquist & Huner, 2003). A reduced photosynthetic activity means much of the radiation absorbed by leaves cannot be utilized for the photosynthetic fixation of CO_2. Hence, the likelihood of water escaping through the stomatal opening (i.e., transpiration) during the carbon uptake process is significantly reduced. In non-forested areas such as grasslands, such a litter layer is usually not developed. In the U.S. croplands, residues are often left on the field after harvesting and can be as effective as forest litter layer. However, the removal of crops after harvesting increases wind speed by reducing ground surface roughness, and thus increases the effective evaporation rate. Another possible reason for the different HI values between the forested and non-forested catchments is the hydraulic redistribution mechanism. With deeper root systems, in the dormant season, trees are able to transport excess water from topsoil down to deeper soil, particularly during nights, hence increasing catchment wetness (Amenu & Kumar, 2008; Brooks et al., 2002; Prieto et al., 2012).

3.3. Further Discussion on the Analytical Framework

λ is the only parameter in our analytical framework, which is closely related to the partitioning of total vaporization (E) into initial (E_0) and continuing vaporization (E_c). In this study, the lambda values are obtained from the monthly HI time series calibration and applied to the multi-scale analysis. Recall that E_0 corresponds to three primary sources where water is easily available for vaporization: Direct evaporation from interception (canopy and litter interception), direct evaporation from the soil surface and temporally stored water in surface depressions, and transpiration from the shallow root zone. The contribution from interception loss accounts for 10%–50% of gross precipitation depending on vegetation types, canopy density, and meteorological conditions (Levia et al., 2011; Miralles et al., 2010; Miralles et al., 2016; Roth et al., 2007; Wang et al., 2007). Thus, it is not unreasonable to infer that direct evaporation from interception contributes to more than 10%–50% of total vaporization. Direct evaporation from surface depressions is a spatiotemporally heterogeneous process mainly driven by surface microtopography (Kamphorst et al., 2000). Surface depressions here mainly refer to those small, unmanaged water bodies embedded either within uplands or river floodplains. They are small yet abundant at the catchment or larger scales (Wu et al., 2019). The temporally stored water in these surface depressions thus plays an important role in catchment hydrological processes, including evaporation (Alexander et al., 2018; Cohen et al., 2016; Golden et al., 2017; Lane et al., 2018; Rajib et al., 2020; Yu & Harbor, 2019). The transpiration component of initial vaporization corresponds to the fast transpiration, which only draws on the upper 50cm of the soil layer where most root biomass is located, and most transpiration occurs (Savenije, 2004). In the U.S., Addor

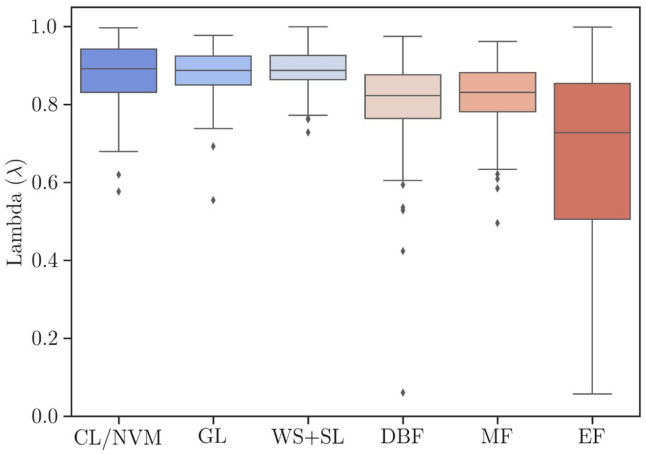

Figure 6. Bot-plot of λ values calibrated at the monthly scale. CL/NVM: Croplands and Croplands/Natural vegetation mosaic; DBF: Deciduous Broadleaf; EF: Evergreen Needleleaf and Broadleaf Forest; MF: Mixed Forests; GL: Grasslands; WS + SL: Savannas, Woody Savannas and Open/Closed Shrublands.

et al. (2017) derived catchment-average root-depth data for 671 catchments based on a global vegetation root distribution model by Zeng (2001), and suggested that, for all catchments (excluding the missing values 24 of 671 catchments), 50% of root biomass is located within the top 25cm soil layer. Globally, Schenk and Jackson (2002b) analyzed 475 profiles for 209 sites in 15 biomes, and showed ~90% of the root system to be in the upper 30cm soil layer across all sites. Initial transpiration from this upper soil layer is thus not trivial and at least comparable to direct evaporation from interception. Overall, each of these three sources of E_0 is nontrivial. E_0 is therefore expected to be a significant, even dominant portion of total vaporization. The value of λ, although it may vary from one catchment to another, should be nontrivial in most catchments. Figure 6 shows the box-plot of calibrated λ values for different biome regimes. The calibrated λ values are more than 0.5 for most catchments, consistent with the above discussion.

What's more interesting from Figure 6 is that the calibrated λ values are relatively lower in the forested catchments, particularly in those EF dominant catchments. The average of calibrated λ values within each biome regime is 0.876, 0.875, 0.886, 0.799, 0.807, and 0.686 for CL/NVM, GL, WS + SL, DBF, MF and EF respectively. The lower λ values in the forested catchments are very likely due to the deeper root systems, which facilitate access to deeper soil water for continuing vaporization. Although overall forest biomes have more interception owing to higher LAI values and understory vegetations, the denser canopy often reduces evaporation from the soil surface by blocking more incoming evaporative (solar) energy and increasing the aerodynamic resistance or vaporization. On the other hand, non-forest biome regimes usually have shallower root systems, which allow for quicker responses to incoming rainfall but less access to deeper soil water for continuing vaporization (Fan et al., 2017; Rore & Stern, 1967). For example, typical root length densities for crop plants are about 6 cm/cm^3 and 1 cm/cm^3 in the surface soil layer and a 50–100 cm deep soil layer, respectively (Glinski & Lipiec, 2018). The GL catchments in this study are mostly located in the Great Plains of North America (Figure 3) and generally fall under water-limited ecosystems (AI > 1.0 for 49 out of 50 GL catchments). In a water-limited biome, root systems are shallower and wider in dry climates and deeper and narrower in cold and wet climates (Schenk & Jackson, 2002a). Hence, GL catchments in this study can be characterized with a shallow and wide root system type. Schenk and Jackson (2002b) data for CONUS grasslands (34 root profiles) show that 90% of the sites have 50% of the root distribution within the top 20cm. A more recent isotopic evapotranspiration partitioning experiment on tallgrass prairie in the Great Plains of North America by Sun et al. (2021) found that the top 10cm soil layer is a major source of the total evapotranspiration during the initial drying periods. Like croplands, high water volume is extracted for transpiration from the topsoil layer; thus, the initial vaporization is a dominant component.

The between-catchment variability of calibrated λ values within each biome regime appears to be higher in the forested catchments, that is, the coefficients of variance are 10.0%, 9.44%, 7.5%, 12.93%, 16.64% and 33.08% for CL/NVM, GL, WS + SL, DBF, MF and EF dominant catchments respectively. This between-catchment variability within each biome regime may be caused by several reasons. First, the difference in the non-dominant proportion of the catchment land cover may be a contributing factor. In each of the 343 selected catchments, we define the dominant cover as the biome type covering >50% of the catchment. For instance, a catchment with 100% DBF cover will behave differently from another with only 60% DBF cover, although both are classified into the same biome regime in this study. Second, the between-catchment variability difference between the forested and non-forested catchments is likely because non-forest biome regimes are often intensive water users featured by high water use efficiency. As such, their behavior (e.g., partitioning of E into E_0 and E_c) is more alike and converging toward optimal rain use efficiency despite the different climate, soil and topographic conditions (Huxman et al., 2004; Troch et al., 2009). Third, the different root systems between the forested and non-forested regimes. In the forested catchments, E_c is usually larger than the non-forested due to deeper roots and easier access to deeper soil water, and thus more sensitive to climate variations because deeper roots allow trees to better cope with climate variations. Last but not least, the variability in type and density of the understory vegetation in the forested catchments

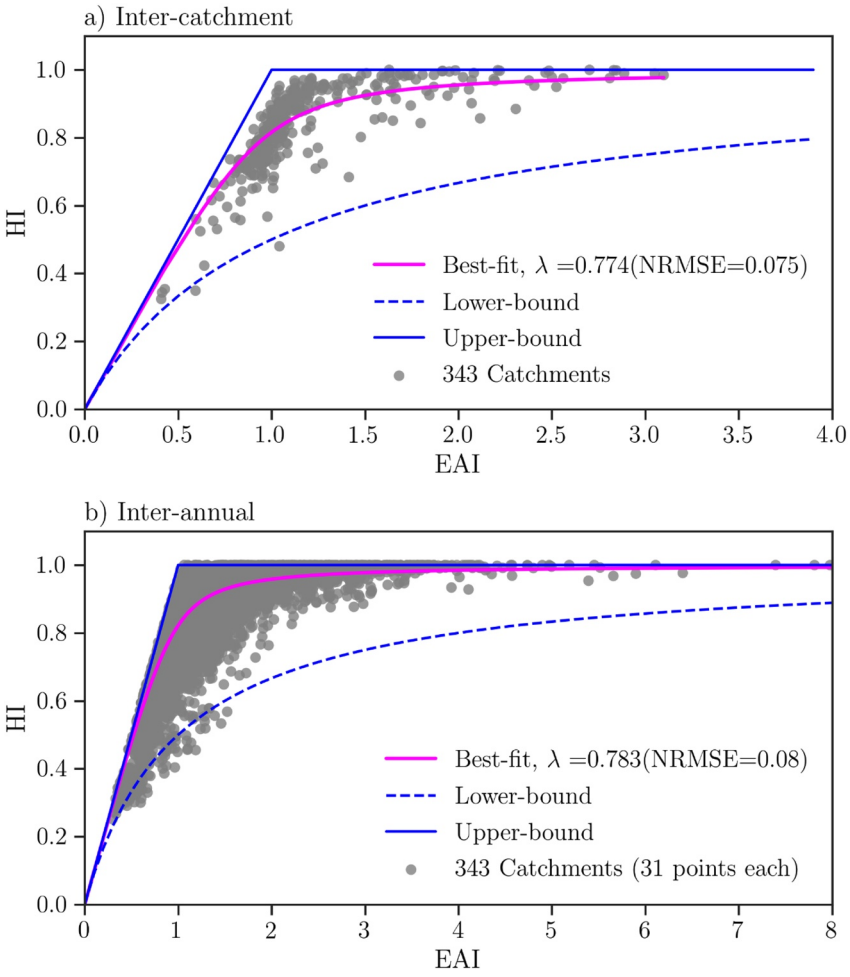

Figure 7. Space-time similarity of HI ~ EAI relationships at the annual scale across different climatic, topographic, and vegetation regimes. (a) Inter-catchment (spatial) variability of HI. Each dot represents one catchment, and HI and EAI are based on the long-term averages in 1982–2012. (b) Inter-annual variability of HI. Each dot represents one year at one catchment (each catchment has 31 dots). The magenta, solid blue, and dashed blue lines correspond to the best-fitted, upper-bound, and lower bound curves using Equation 13, respectively.

may also contribute to this between-catchment variability. The types of understory can be trees, shrubs, or herbaceous vegetation. For instance, if trees dominate the understory, more water is likely to be extracted from deeper soil (especially during the summer season) than an understory dominated by nonperennial herbaceous vegetation with shallow roots. Moreover, the understory also affects soil evaporation since a denser understory will more likely block solar radiation from reaching the soil surface.

4. Emergent Patterns and Theoretical Insights

Upon successful validation, we further investigate the analytical framework's capacity to help detect and explain emergent patterns in HI's spatiotemporal variations at different temporal scales. Note here we define space-time similarity as the similarity between a spatial (between-catchment) variability and a temporal (within-catchment but between different years or months) trend.

4.1. Space-Time Similarity in the Between- and Within-Catchment Trends of HI

Figure 7a shows that the analytical framework can well capture HI's inter-catchment variability, that is, the increasing trend of HI from wetter to drier catchments. Here each dot in Figure 7a represents a pair of

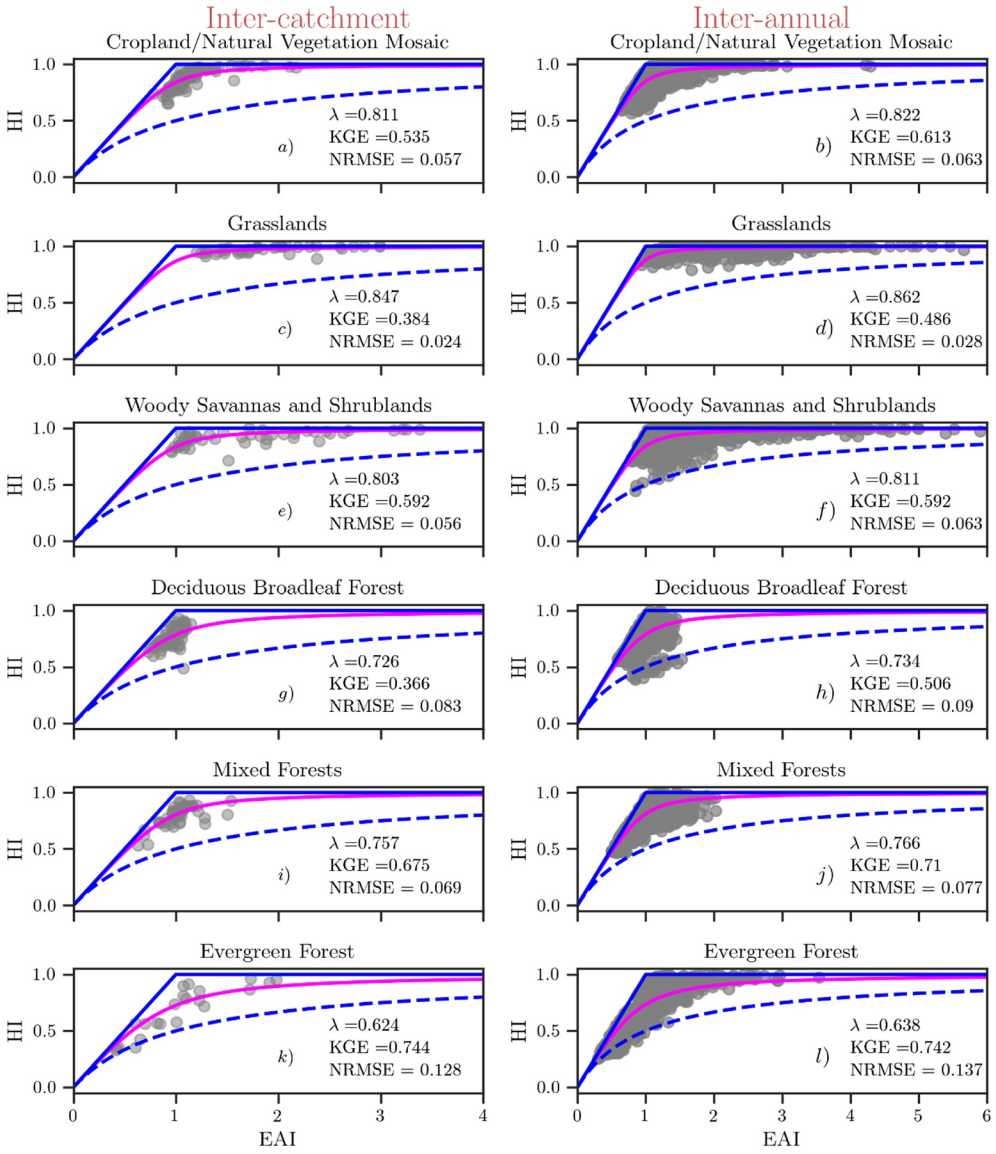

Figure 8. Space-time similarity of HI ~ EAI relationships at the annual scale for different vegetation regimes. On the left-hand side (a, c, e, g, i, j), inter-catchment (spatial) variability of long-term HI. Each dot represents one catchment, and HI and EAI were based on the long-term averages in 1982–2012. On the right-hand side (b, d, f, h, j, l), annual HI's inter-annual variability. Each dot represents one year at one catchment (each catchment has 31 dots). The magenta, solid blue, and dashed blue lines correspond to the best-fitted, upper-bound, and lower bound curves using Equation 13, respectively.

estimated long-term HI and EAI values for one of the 343 catchments. The magenta line is the "analytical" curve fitted using Equation 13, with a calibrated λ value of 0.774 and an NRMSE value of 0.075. Moreover, the analytical framework also captures the between-year variability of HI very well, i.e., increasing trend of HI from wetter to drier years, as shown in Figure 7b. Here each dot represents a pair of "estimated" annual HI and EAI values for one catchment and one year in 1982–2012. The analytical curve is fitted again using Equation 13, achieving a calibrated λ value of 0.783, and the NRMSE value is 0.08. The calibrated λ value at the long-term scale, 0.774, is quite close to that at the annual scale, 0.783, suggesting a space-time similarity of HI increasing trend from wetter catchments (years) to drier catchments (years).

Figure 8 further explores this space-time similarity but for different biome regimes. Again, the closeness between the long-term and annual calibrated λ values across different vegetation types confirms the space-

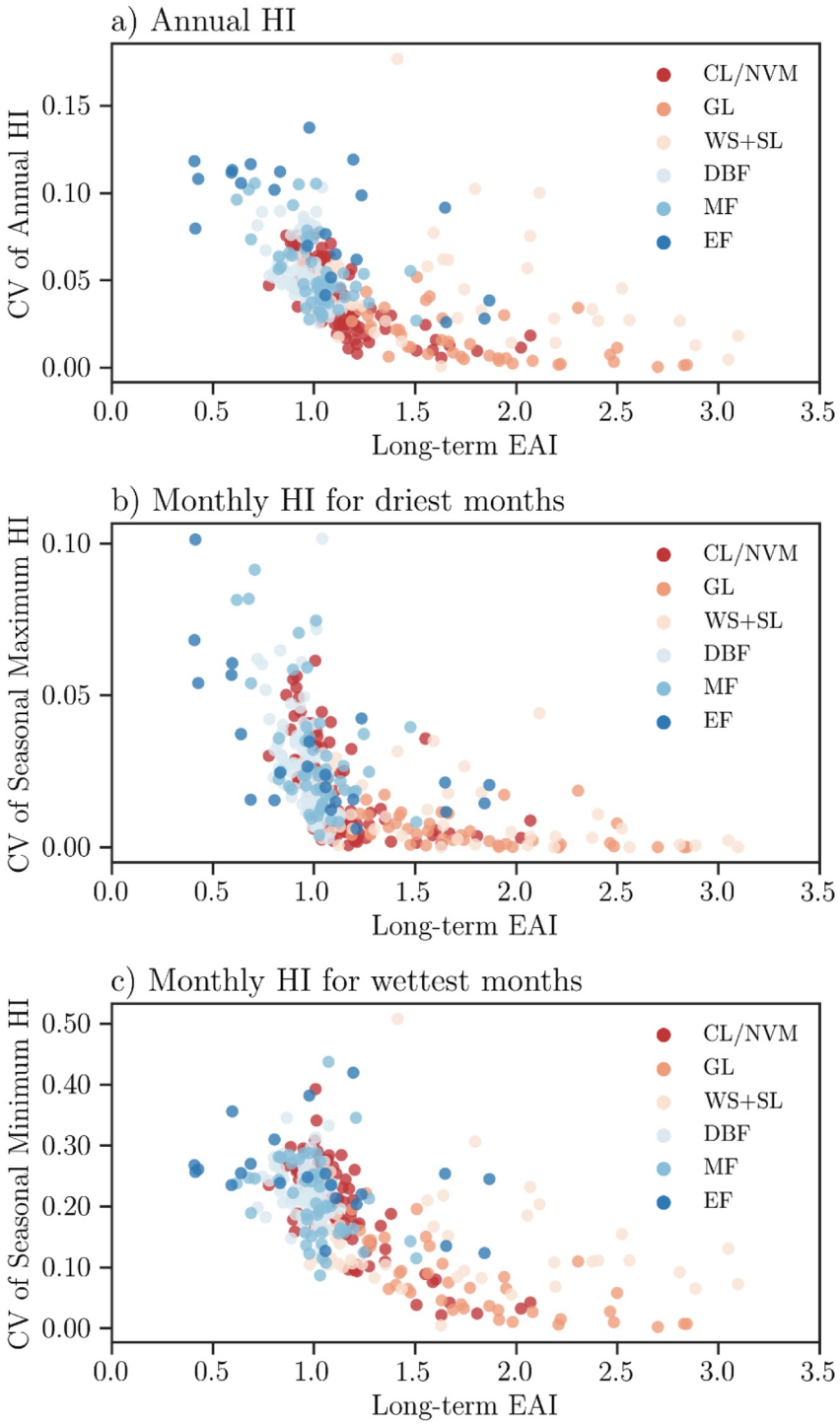

Figure 9. Inter-annual variability of (a) annual HI values, (b) monthly HI values but for the driest month only from each year, and (c) monthly HI values but for the wettest month only from each year. Each dot here represents one catchment.

time similarity both empirically and theoretically. It appears that most non-forest catchments are in an ecologically dry state, that is, EAI > 1.0 for both between-catchment and between-year cases. Under such a dry state, these non-forest biome regimes tend to operate toward the optimal water use efficiency, leading to the convergence of HI values toward 1.0. The variability of HI in these non-forested catchments is thus

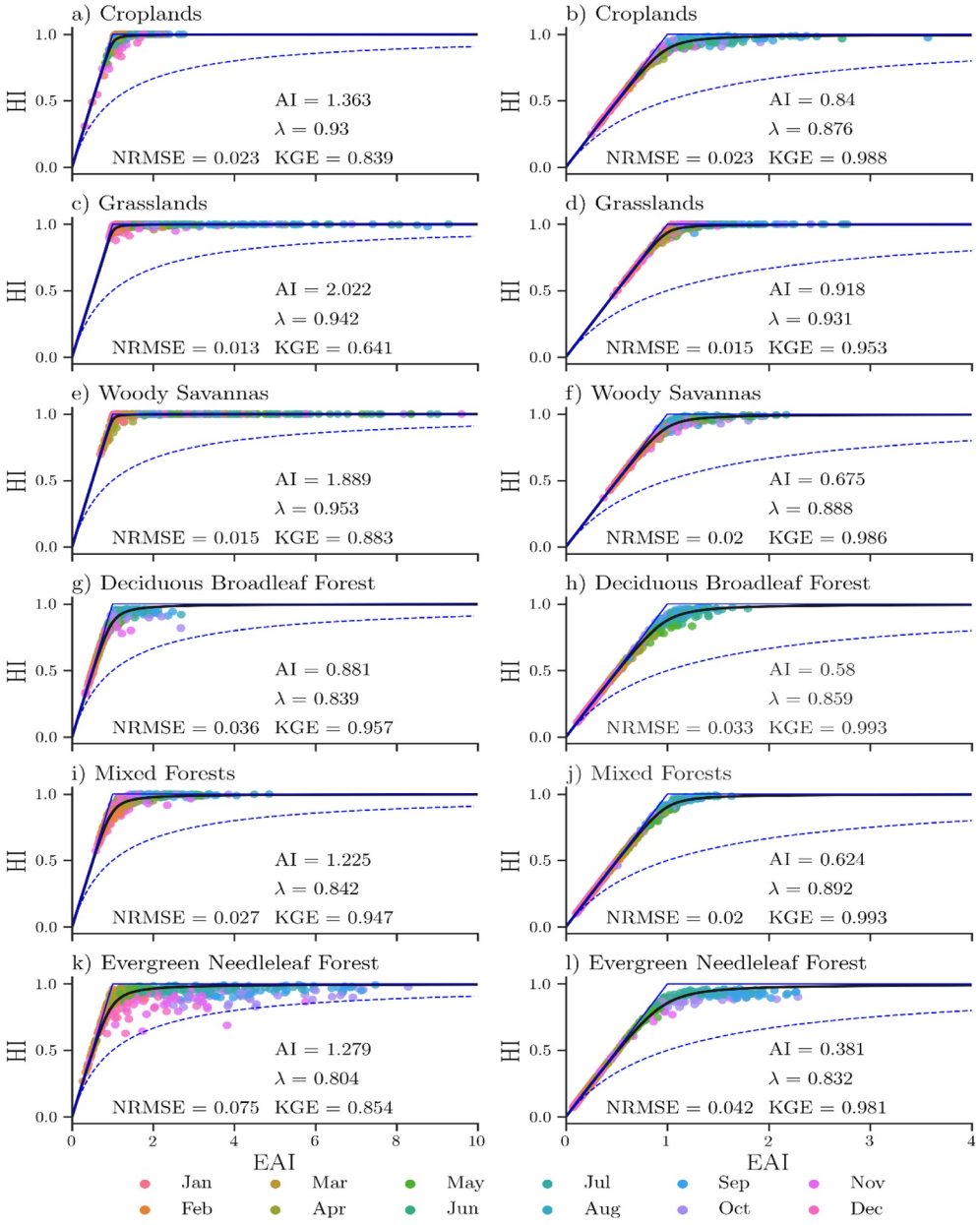

Figure 10. Intra-annual variability of monthly HI within individual catchments in 1982–2012. The black, solid blue, and dashed blue lines correspond to the best-fitted, upper-bound, and lower bound curves using Equation 13 respectively. The corresponding USGS gage ID for the catchments are, (a) 5123400, (b) 3241500, (c) 6447000, (d) 6917000, (e) 9505350, (f) 2481000, (g) 3173000, (h) 1413500, (i) 2212600, (j) 1162500, (k) 11162500, and l) 14325000.

small. The forested catchments nonetheless do not have such a preference. The DBF catchments have the narrowest range of EAI values, followed by the MF and then EF dominant catchments. Overall, the variability of annual HI decreases from wetter to drier states, as shown in Figure 9a.

More interestingly, the above space-time similarity exists not only at the annual scale but also at the monthly scale, as shown in Figures 10 and 11. Figure 10 shows that the monthly HI values increase from the wetter to drier months as captured by both the empirical data points and theoretical curves at each representative catchment. Overall, the evapotranspiration in the growing season is higher than the dormant season and dominated by plant transpiration over evaporation from soil and interception. Correspondingly, the monthly HI values in the growing season are generally higher than those in the dormant season.

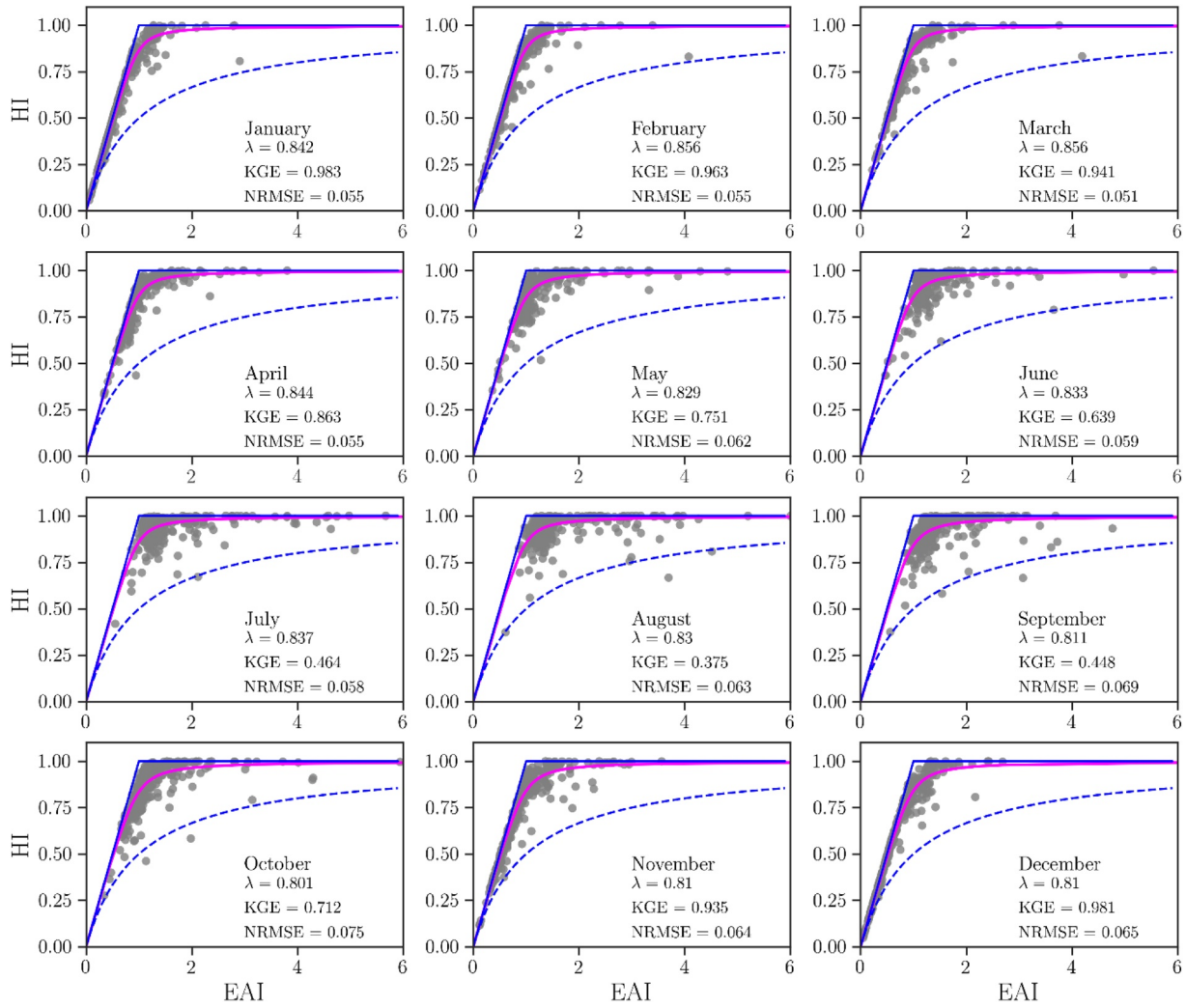

Figure 11. Intra-annual variability of mean-monthly HI between catchments. The magenta, solid blue, and dashed blue lines correspond to the best-fitted, upper-bound, and lower bound curves using Equation 13, respectively.

Figure 11 confirms this trend of intra-annual variability across all 343 catchments. The 12 subplots in Figure 11 are corresponding to the 12 months in a calendar year. Each dot represents one catchment, for example, in Figure 10a, the January HI value for a catchment is calculated as a ratio of the average of January precipitation in 1982–2012 over the average of January catchment wetting. This way, HI's intra-annual variability manifests as the difference between the subpanels in Figure 11. Overall, in the growing season, particularly July-September, the HI values are preferentially distributed in the ecologically dry state, that is, EAI > 1, hence the variability of monthly HI values is relatively small, as more clearly shown in Figure 9b. In the dormant season, particularly December–February, the HI values are more distributed in the ecologically wet state, and the variability of monthly HI values is relatively larger, as also shown in Figure 9c.

Within each panel in Figure 11, the between-catchment variability is well captured by the theoretical curves. For example, in the subpanel corresponding to May, the HI values increase from those catchments with a drier May to those with a wetter May in an average sense. Within each subpanel, a calibrated λ value is chosen to best capture the inter-catchment variability. The calibrated λ values are quite similar among the subpanels, that is, varying in a very narrow range 0.81–0.86, suggesting similar inter-catchment variability across different seasons.

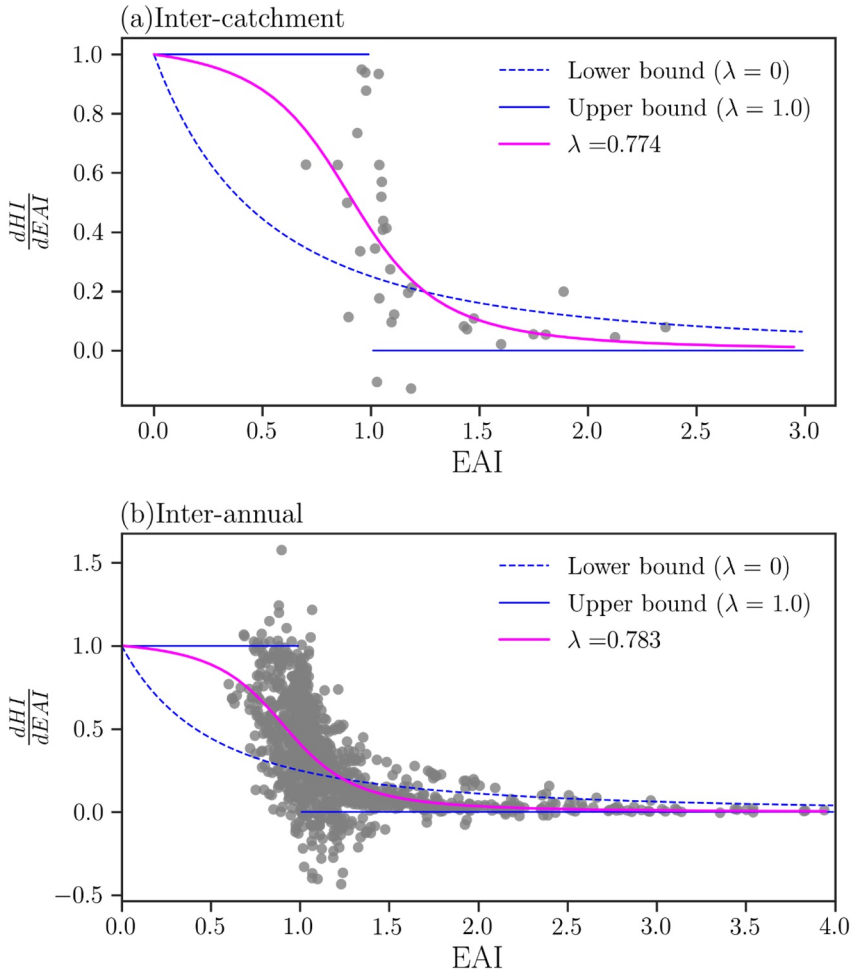

Figure 12. Space-time similarity of d (HI)/d (EAI)~EAI relationships at the annual scale across different climatic, topographic, and vegetation regimes. (a) Between-catchment (spatial) variability. Each dot represents one catchment, and HI and EAI are based on the long-term averages in 1982–2012. (b) Between-year (inter-annual) variability. Each dot represents one year at one catchment (each catchment has 31 dots). A bin size of ten (10 dots per bin) is used for both (a) and (b). The magenta, solid blue, and dashed blue lines correspond to the best-fitted, upper-bound, and lower bound curves using Equation 14, respectively.

4.2. Space-Time Similarity in the Increasing Rate of HI With EAI

So far, we have verified the increase of HI with EAI both theoretically (based on Equation 13) and empirically (using the "estimated" HI and EAI values) with a space-time similarity. Next, we examine the spatio-temporal variability of the changing rates of HI, or the slopes in the $HI \sim EAI$ relationships, quantified using $d(HI) / d(EAI)$ as in Equation 14.

Figure 12 shows the $d(HI) / d(EAI)$ at the long-term and annual scales corresponding to Figure 7. We first divide all the "estimated" $HI \sim EAI$ values in Figure 7 into several bins, each bin containing 10 pairs of "estimated" $HI \sim EAI$ values. We then perform a linear regression within each bin, and the resulting slope is used as the estimated $d(HI) / d(EAI)$ value, shown as one dot in Figure 12. Note that we test the bin size from 5 to 10 for different data sizes, and the patterns remain similar. We, therefore, use a bin size of 10 in the rest of the Figures. The theoretical curves in Figure 12 are derived based on Equation 14 using the same λ values as in Figure 7.

Figure 12 suggests that $d(HI) / d(EAI)$ decreases with increase in EAI in a space-time similar way, that is, it decreases both from wetter to drier catchments and from wetter to drier years, but following the same

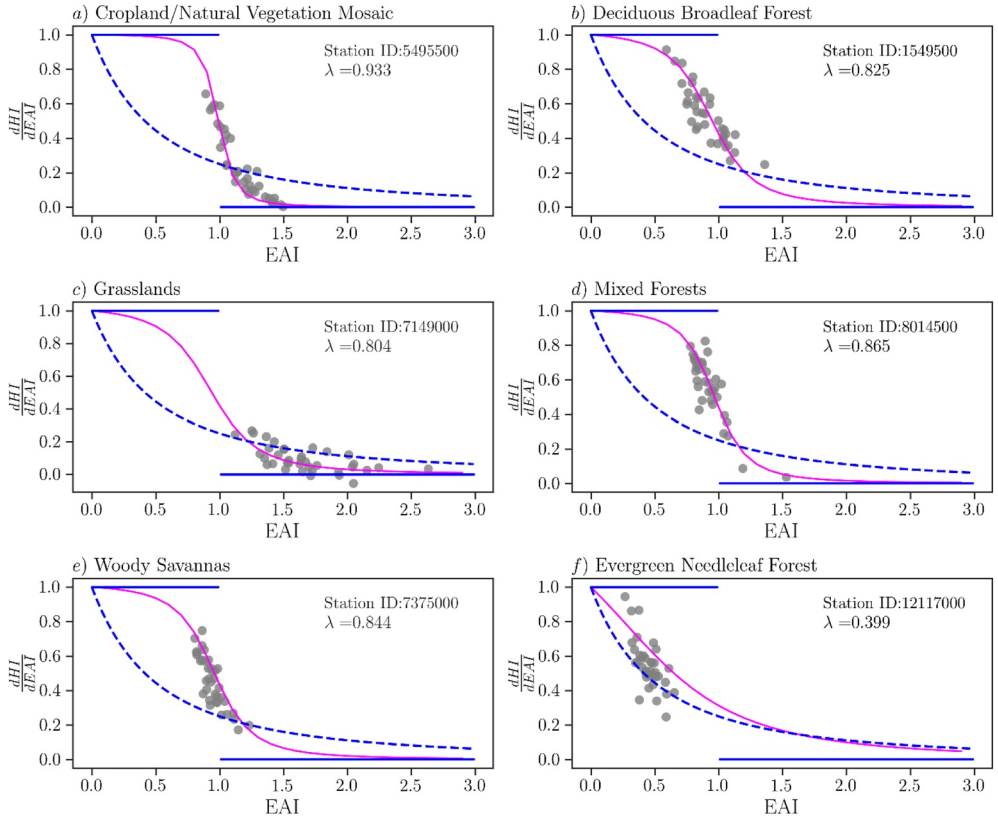

Figure 13. d (HI)/d (EAI)~EAI relationships at the monthly scale for individual catchments (1982–2012). A bin size of 10 is used to compute the empirical d (HI)/d (EAI). The magenta, solid blue, and dashed blue lines correspond to the best-fitted, upper-bound, and lower bound curves using Equation 14, respectively.

decreasing pattern. This $d(HI) / d(EAI)$ decreasing pattern can be roughly characterized as an *S*-shape and divided into three stages: (a) $d(HI) / d(EAI)$ decreases slowly and remains relatively high for $0 \le EAI < \sigma_1$; (b) $d(HI) / d(EAI)$ decreases quickly for $\sigma_1 \le EAI < \sigma_2$; and (c) $d(HI) / d(EAI)$ decreases slowly but remains relatively low for $EAI > \sigma_2$. σ_1 and σ_2 are divisions between the three stages and cannot be accurately defined since the transitions from Stage (a) to (b) and from State (b) to (c) are both gradual instead of abrupt. There are some dots in Figure 12 beyond the theoretical upper $(d(HI) / d(EAI) = 1)$ or lower $(d(HI) / d(EAI) = 0)$ limits, and we attribute these to the uncertainties embedded in the CAMELS data. We do not produce a $d(HI) / d(EAI)$ plot corresponding to Figure 8 using the same binning method because of the number of $HI \sim EAI$ pairs is too small.

Figures 13 and 14 examine the $d(HI) / d(EAI)$, or slope values of the $HI \sim EAI$ relationships at the monthly scale corresponding to Figures 10 and 11, respectively. Similar to Figure 12, the $d(HI) / d(EAI)$ values decrease with increase in EAI following an S-shape pattern across both time (Figure 13) and space (Figure 14), hence suggesting a space-time similarity at the monthly scale.

5. Summary and Conclusions

In this study, we present an analytical framework of HI as a single function of ecological aridity index (EAI) (see Figures 1 and 2) based on the Generalized Proportionality Hypothesis. We successfully validate it over the long-term, annual, and monthly scales across various regimes of climate, vegetation, soil, and topography (see Figures 3–6). λ, as a direct indicator of catchment wetting (or effective water storage) partitioning, is no less than 0.5 over most of the 343 catchments over the contiguous United States, indicating the im-

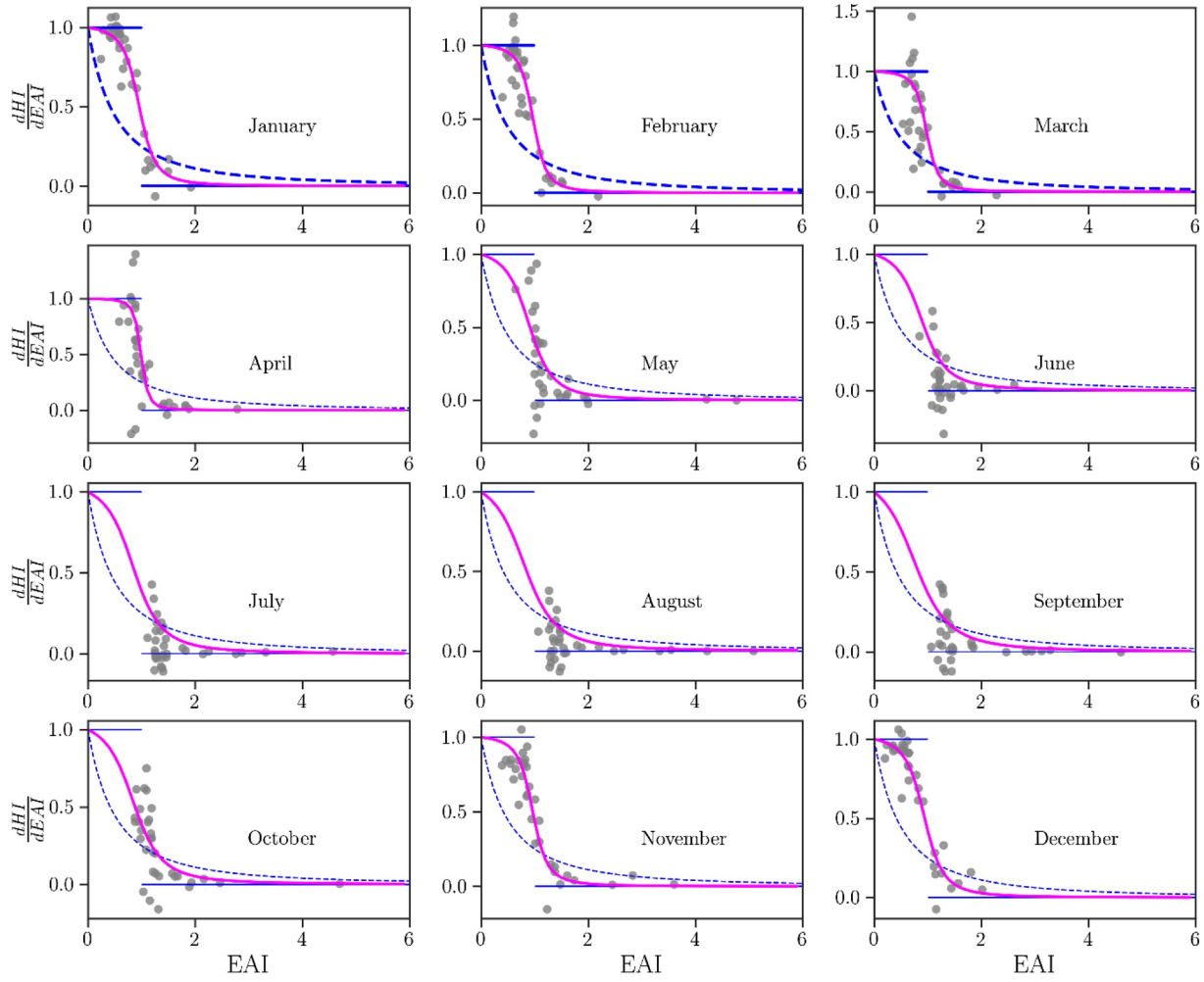

Figure 14. Space-time similarity: d (HI)/d (EAI)~EAI of Monthly means of the Horton Index across spaces. A bin size of 10 is used to compute the empirical d (HI)/d (EAI). The magenta, solid blue, and dashed blue lines correspond to the best-fitted, upper-bound, and lower bound curves using Equation 14, respectively.

portance of catchments' initial responses to storm events in the form of direct evaporation from vegetation interception and ground surface and transpiration from the shallow root zone. We suggest that different biome regimes exert different levels of control on not only partitioning of catchment wetting (or total water storage) into vertical vaporization and lateral baseflow but also partitioning of vaporization into initial and continuing components.

Facilitated with this analytical framework, we find that there is an emergent space-time similarity between the regional (inter-catchment) and intra-annual variability of HI, expressed in terms of the $HI \sim EAI$ relationships. The space-time similarity of HI's intra-annual variability appears to resemble that of HI's inter-annual variability (see Figures 7–10), suggesting that HI increases from wetter to drier places, years, or months in a similar fashion. The analytical framework can explain these space-time similarity patterns in a unified way, i.e., HI increases with EAI following a similar curve provided by Equation 13. More interestingly, we find that this space-time similarity also exists in the slopes of the $HI \sim EAI$ relationships, quantified by an S-shaped curve of $d(HI) / d(EAI) \sim EAI$ relationship given by Equation 14. Under very dry conditions, HI approaches its theoretical maximum, 1.0, but with decreasing regional or temporal (inter- and intra-annual) variability in a space-time symmetric fashion. Equation 14 thus shed some light on the previous finding of HI's inter-catchment and inter-year constancy (Horton, 1933; Troch et al., 2009) under dry conditions, and further extend it to HI's intra-annual variability for different biome regimes.

This analytical framework opens the door and/or paves the way to many exciting opportunities to advance our understanding of water-plant-soil-climate interactions, including but not limited to:

- HI is a better indicator than AI for vegetation water use. HI captures the partitioning of soil moisture storage, which is directly available to vegetation. AI (in the framework of the Budyko formula) captures the partitioning of precipitation into runoff and E, and the runoff part includes surface runoff which is not available to vegetation. The analytical framework of HI can thus be a useful tool to explore quantitative connections between ecohydrology and hydrology at the catchment scale (e.g., over a few catchments) or regional scale (e.g., over a large number of catchments in a region)
- In this study, we assume that GPH is valid at the monthly scale for the partitioning of catchment wetting into vaporization and baseflow. We validate this assumption by showing empirical evidence that our analytical framework has successfully reproduced intra-annual variability of HI across over 340 catchments. It is nevertheless worthy to further explore to what extent GPH can be applied. Given the fact that the SCS-CN method is essentially applicable at the event scale, it is feasible to explore whether and how GPH can be applied to the 2nd-stage of hydrologic partitioning at the event scale and how vegetation may play a role in it
- This analytical framework can be used as a first-order constraint to the simulated ecological and hydrological responses from hydrological, land surface, and earth system models, helping prompt a balanced, effective representation of hydrological and ecological processes and their interactions and hence reducing the simulation uncertainties
- Our analytical framework may be used to improve the parameterization of hydrologic models due to its common theoretical basis with the SCS-CN method, that is, GPH. Furthermore, the SCS-CN method is suggested to have a similar physical basis with the *abcd* model (Wang & Tang, 2014) and Variability Infiltration Model (Wang, 2018). There is thus a promising potential to help better estimate the runoff parameters, for instance, according to dominant vegetation cover in each of the spatial units in these models
- The emergent space-time similarity patterns may be used as empirical evidence to advancing our understanding of Horton's hypothesis that vegetation practices maximization of productivity relative to available water (Horton, 1933). Despite the highly nonlinear vegetation dynamics and spatiotemporal heterogeneity in climate, soil, and topographic conditions, it appears that vegetation maximum productivity may function as an organizing principle and lead to a convergence of plant-soil-atmosphere interactions, which manifests in the form of emergent patterns presented here

We suggest that the analytical framework and emergent patterns have important implications to improving understanding and modeling of ecological and hydrological processes and their interactions at the catchment and larger scales. More broadly, the findings from this study suggest the promising potential of Horton Index as a conceptual yet quantitative framework for exploring the links between catchment water balance and vegetation dynamics across multiple scales in space (catchment to regional scales) and time (event to long-term scales).

Data Availability Statement

All the data used in this study are from the Catchment Attributes and MEteorology for Large-sample Studies (CAMELS) data set, which can be accessed at https://ral.ucar.edu/solutions/products/camels.

Acknowledgments
The authors sincerely thank the editors, Antônio Alves Meira Neto, and the other two anonymous reviewers, whose constructive comments have helped elevate the study significantly. This research is supported by the U.S. Department of Energy Office of Science Biological and Environmental Research as part of the Earth System Model Development program through the Energy Exascale Earth System Model (E3SM) project and the U.S. National Science Foundation (EAR #1804560).

References

Adams, W. W., Zarter, C. R., Ebbert, V., & Demmig-Adams, B. (2004). Photoprotective Strategies of Overwintering Evergreens. *BioScience*, *54*(1), 41–49. https://doi.org/10.1641/0006-3568(2004)054[0041:psooe]2.0.co;2

Addor, N., Newman, A. J., Mizukami, N., & Clark, M. P. (2017). The CAMELS data set: Catchment attributes and meteorology for large-sample studies. *Hydrology and Earth System Sciences*, *21*(10), 5293–5313. https://doi.org/10.5194/hess-21-5293-2017

Alexander, L. C., Fritz, K. M., Schofield, K. A., Autrey, B. C., DeMeester, J. E., Golden, H. E., et al. (2018). Featured Collection Introduction: Connectivity of Streams and Wetlands to Downstream Waters. *Journal of the American Water Resources Association*, *54*(2), 287–297. https://doi.org/10.1111/1752-1688.12630

Amenu, G. G., & Kumar, P. (2008). A model for hydraulic redistribution incorporating coupled soil-root moisture transport. *Hydrology and Earth System Sciences*, *12*(1), 55–74. https://doi.org/10.5194/hess-12-55-2008

Arciniega-Esparza, S., Breña-Naranjo, J. A., & Troch, P. A. (2017). On the connection between terrestrial and riparian vegetation: The role of storage partitioning in water-limited catchments. *Hydrological Processes*, *31*(2), 489–494. https://doi.org/10.1002/hyp.11071

Brooks, J. R., Meinzer, F. C., Coulombe, R., & Gregg, J. (2002). Hydraulic redistribution of soil water during summer drought in two contrasting Pacific Northwest coniferous forests. *Tree Physiology*, *22*(15–16), 1107–1117. https://doi.org/10.1093/treephys/22.15-16.1107

Brooks, P. D., Troch, P. A., Durcik, M., Gallo, E., & Schlegel, M. (2011). Quantifying regional scale ecosystem response to changes in precipitation: Not all rain is created equal. *Water Resources Research*, *47*(7), 1–13. https://doi.org/10.1029/2010WR009762

Budyko, M. I. (1974). *Climate and life*. Academic Press.

Cohen, M. J., Creed, I. F., Alexander, L., Basu, N. B., Calhoun, A. J. K., Craft, C., et al. (2016). Do geographically isolated wetlands influence landscape functions? *Proceedings of the National Academy of Sciences of the United States of America*, *113*, 1978–1986. https://doi.org/10.1073/pnas.1512650113

Fan, Y., Miguez-Macho, G., Jobbágy, E. G., Jackson, R. B., & Otero-Casal, C. (2017). Hydrologic regulation of plant rooting depth. *Proceedings of the National Academy of Sciences of the United States of America*, *114*(40), 10572–10577. https://doi.org/10.1073/pnas.1712381114

Fu, B. P. (1981). On the calculation of the evaporation from land surface. *Scientia Atmospherica Sinica*, *5*(1), 23–31.

Glinski, J., & Lipiec, J. (2018). Soil physical conditions and plant roots. In *Soil physical conditions and plant roots*. CRC Press. https://doi.org/10.1201/9781351076708

Golden, H. E., Creed, I. F., Ali, G., Basu, N. B., Neff, B. P., Rains, M. C., et al. (2017). Integrating geographically isolated wetlands into land management decisions. *Frontiers in Ecology and the Environment*, *15*(6), 319–327. https://doi.org/10.1002/fee.1504

Gomyo, M., & Kuraji, K. (2016). Effect of the litter layer on runoff and evapotranspiration using the paired watershed method. *Journal of Forest Research*, *21*(6), 306–313. https://doi.org/10.1007/s10310-016-0542-5

Guardiola-Claramonte, M., Troch, P. A., Ziegler, A. D., Giambelluca, T. W., Durcik, M., Vogler, J. B., & Nullet, M. A. (2010). Hydrologic effects of the expansion of rubber (Hevea brasiliensis) in a tropical catchment. *Ecohydrology*, *3*(3), 306–314. https://doi.org/10.1002/eco.110

Gupta, H. V., Kling, H., Yilmaz, K. K., & Martinez, G. F. (2009). Decomposition of the mean squared error and NSE performance criteria: Implications for improving hydrological modeling. *Journal of Hydrology*, *377*(1–2), 80–91. https://doi.org/10.1016/j.jhydrol.2009.08.003

Harman, C. J., Troch, P. A., & Sivapalan, M. (2011). Functional model of water balance variability at the catchment scale: 2. Elasticity of fast and slow runoff components to precipitation change in the continental United States. *Water Resources Research*, *47*(2), 1–12. https://doi.org/10.1029/2010WR009656

Hooshyar, M., & Wang, D. (2016). An analytical solution of Richards' equation providing the physical basis of SCS curve number method and its proportionality relationship. *Water Resources Research*, *52*(8), 6611–6620. https://doi.org/10.1002/2016WR018885

Horton, R. E. (1933). The Rôle of infiltration in the hydrologic cycle. *Transactions of AGU*, *14*(1), 446–460. https://doi.org/10.1029/TR014i001p00446

Hufkens, K., Keenan, T. F., Flanagan, L. B., Scott, R. L., Bernacchi, C. J., Joo, E., et al. (2016). Productivity of North American grasslands is increased under future climate scenarios despite rising aridity. *Nature Climate Change*, *6*(7), 710–714. https://doi.org/10.1038/nclimate2942

Huxman, T. E., Smith, M. D., Fay, P. A., Knapp, A. K., Shaw, M. R., Loik, M. E., et al. (2004). Convergence across biomes to a common rain-use efficiency. *Nature*, *429*(6992), 651–654. https://doi.org/10.1038/nature02561

Kamphorst, E. C., Jetten, V., Guérif, J., Pitk a ¨ nen, J., Iversen, B. V., Douglas, J. T., & Paz, A. (2000). Predicting Depressional Storage from Soil Surface Roughness. *Soil Science Society of America Journal*, *64*(5), 1749–1758. https://doi.org/10.2136/sssaj2000.6451749x

Kukal, M. S., & Irmak, S. (2018). U.S. agro-climate in 20th century: Growing degree days, first and last frost, growing season length, and impacts on crop yields. *Scientific Reports*, *8*(1), 1–14. https://doi.org/10.1038/s41598-018-25212-2

Lane, C. R., Leibowitz, S. G., Autrey, B. C., LeDuc, S. D., & Alexander, L. C. (2018). Hydrological, physical, and chemical functions and connectivity of non-floodplain wetlands to downstream waters: A review. *Journal of the American Water Resources Association*, *54*(2), 346–371. https://doi.org/10.1111/1752-1688.12633

Levia, D. F., Carlyle-Moses, D. E., & Tanaka, T. (2011). Forest hydrology and biogeochemistry : Synthesis of past research and future directions Ecological studies (Vol. 216). Springer Netherlands. https://doi.org/10.1007/978-94-007-1363-5

L'vovich, M. I. (1979). World water resources and their future Special publications series (Vol. 13). American Geophysical Union. https://doi.org/10.1029/SP013

Miralles, D. G., Gash, J. H., Holmes, T. R. H., De Jeu, R. A. M., & Dolman, A. J. (2010). Global canopy interception from satellite observations. *Journal of Geophysical Research*, *115*(16), 1–8. https://doi.org/10.1029/2009JD013530

Miralles, D. G., Jiménez, C., Jung, M., Michel, D., Ershadi, A., McCabe, M. F., et al. (2016). The WACMOS-ET project - Part 2: Evaluation of global terrestrial evaporation data sets. *Hydrology and Earth System Sciences*, *20*(2), 823–842. https://doi.org/10.5194/hess-20-823-2016

Nathan, R. J., & McMahon, T. A. (1990). Evaluation of automated techniques for base flow and recession analyses. *Water Resources Research*, *26*(7), 1465–1473. https://doi.org/10.1029/WR026i007p01465

Newman, A. J., Clark, M. P., Sampson, K., Wood, A., Hay, L. E., Bock, A., et al. (2015). Development of a large-sample watershed-scale hydrometeorological data set for the contiguous USA: Data set characteristics and assessment of regional variability in hydrologic model performance. *Hydrology and Earth System Sciences*, *19*(1), 209–223. https://doi.org/10.5194/hess-19-209-2015

Ol'dekop, E. M. (1911). On evaporation from the surface of river basins. In *Transactions on meteorological observations*. Tartu.

Öquist, G., & Huner, N. P. A. (2003). Photosynthesis Ofoverwinteringevergreenplants. *Annual Review of Plant Biology*, *54*, 329–355. https://doi.org/10.1146/annurev.arplant.54.072402.115741

Ponce, V. M., & Shetty, A. V. (1995a). A conceptual model of catchment water balance: 1. Formulation and calibration. *Journal of Hydrology*, *173*(1–4), 27–40. https://doi.org/10.1016/0022-1694(95)02739-C

Ponce, V. M., & Shetty, A. V. (1995b). A conceptual model of catchment water balance: 2. Application to runoff and baseflow modeling. *Journal of Hydrology*, *173*(1–4), 41–50. https://doi.org/10.1016/0022-1694(95)02745-B

Prieto, I., Armas, C., & Pugnaire, F. I. (2012). Water release through plant roots: New insights into its consequences at the plant and ecosystem level. *New Phytologist*, *193*, 830–841. https://doi.org/10.1111/j.1469-8137.2011.04039.x

Rajib, A., Golden, H. E., Lane, C. R., & Wu, Q. (2020). Surface Depression and Wetland Water Storage Improves Major River Basin Hydrologic Predictions. *Water Resources Research*, *56*(7), 1–19. https://doi.org/10.1029/2019WR026561

Rasmussen, C. (2012). Thermodynamic constraints on effective energy and mass transfer and catchment function. *Hydrology and Earth System Sciences*, *16*(3), 725–739. https://doi.org/10.5194/hess-16-725-2012

Rore, C. W., & Stern, W. R. (1967). Determination of withdrawal of water from soil by crop roots as a function of depth and time. *Journal of Agricultural Meteorology*, *23*(3), 130–130137. https://doi.org/10.2480/agrmet.23.130

Roth, B. E., Slatton, K. C., & Cohen, M. J. (2007). On the potential for high-resolution lidar to improve rainfall interception estimates in forest ecosystems. *Frontiers in Ecology and the Environment*, *5*(8), 421–428. https://doi.org/10.1890/060119.1

Sakaguchi, K., & Zeng, X. (2009). Effects of soil wetness, plant litter, and under-canopy atmospheric stability on ground evaporation in the Community Land Model (CLM3.5). *Journal of Geophysical Research*, *114*(1), 1–14. https://doi.org/10.1029/2008JD010834

Savenije, H. H. G. (2004). The importance of interception and why we should delete the term evapotranspiration from our vocabulary. *Hydrological Processes*, *18*(8), 1507–1511. https://doi.org/10.1002/hyp.5563

Schaefli, B., Van Der Ent, R. J., Woods, R., & Savenije, H. H. G. (2012). An analytical model for soil-atmosphere feedback. *Hydrology and Earth System Sciences*, *16*(7), 1863–1878. https://doi.org/10.5194/hess-16-1863-2012

Schenk, H. J., & Jackson, R. B. (2002a). Rooting depths, lateral root spreads and below-ground/above-ground allometries of plants in water-limited ecosystems. *Journal of Ecology*, *90*(3), 480–494. https://doi.org/10.1046/j.1365-2745.2002.00682.x

Schenk, H. J., & Jackson, R. B. (2002b). The global biogeography of roots. *Ecological Monographs*, *72*(3), 311–328. https://doi.org/10.1890/0012-9615(2002)072[0311:TGBOR]2.0.CO;2

Schlesinger, W. H., & Jasechko, S. (2014). Transpiration in the global water cycle. *Agricultural and Forest Meteorology*, *189–190*, 115–117. https://doi.org/10.1016/j.agrformet.2014.01.011

SCS. (1985). *National engineering handbook. Section 4, Hydrology*. DC: U.S. Dept. of Agriculture, Soil Conservation Service; Reproduced by National Technical Information Service. Retrieved from http://catalog.hathitrust.org/Record/100889125

Sivapalan, M., Yaeger, M. A., Harman, C. J., Xu, X., & Troch, P. A. (2011). Functional model of water balance variability at the catchment scale: 1. Evidence of hydrologic similarity and space-time symmetry. *Water Resources Research*, *47*(2), 1–18. https://doi.org/10.1029/2010WR009568

Song, J., Willmott, C. J., & Hanson, B. (1997). Simulating the surface energy budget over the Konza Prairie with a mesoscale model. *Agricultural and Forest Meteorology*, *87*(2–3), 105–118. https://doi.org/10.1016/S0168-1923(97)00023-3

Sun, X., Wilcox, B. P., Zou, C. B., Stebler, E., West, J. B., & Wyatt, B. (2021). Isotopic partitioning of evapotranspiration in a mesic grassland during two wetting-drying episodes. *Agricultural and Forest Meteorology*, *301–302*, 108321. https://doi.org/10.1016/j.agrformet.2021.108321

Tang, Y., & Wang, D. (2017). Evaluating the role of watershed properties in long-term water balance through a Budyko equation based on two-stage partitioning of precipitation. *Water Resources Research*, *53*(5), 4142–4157. https://doi.org/10.1002/2016WR019920

Thompson, S. E., Harman, C. J., Troch, P. A., Brooks, P. D., & Sivapalan, M. (2011). Spatial scale dependence of ecohydrologically mediated water balance partitioning: A synthesis framework for catchment ecohydrology. *Water Resources Research*, *47*(5), 1–20. https://doi.org/10.1029/2010WR009998

Troch, P. A., Dwivedi, R., Liu, T., Meira Neto, A. A., Roy, T., Valdés-Pineda, R., et al. (2018). Catchment-scale groundwater recharge and vegetation water use efficiency. *Hydrology and Earth System Sciences Discussions*, 1–46. https://doi.org/10.5194/hess-2018-449

Troch, P. A., Martinez, G. F., Pauwels, V. R. N., Durcik, M., Sivapalan, M., Harman, C., et al. (2009). Climate and vegetation water use efficiency at catchment scales. *Hydrological Processes*, *23*(16), 2409–2414. https://doi.org/10.1002/hyp.7358

Voepel, H., Ruddell, B., Schumer, R., Troch, P. A., Brooks, P. D., Neal, A., et al. (2011). Quantifying the role of climate and landscape characteristics on hydrologic partitioning and vegetation response. *Water Resour. Res.*, *47*(8), 1–13. https://doi.org/10.1029/2010WR009944

Wang, D. (2018). A new probability density function for spatial distribution of soil water storage capacity leads to SCS curve number method. *Hydrology and Earth System Sciences Discussions*, *22*, 1–31. https://doi.org/10.5194/hess-2018-32

Wang, D., & Tang, Y. (2014). A one-parameter Budyko model for water balance captures emergent behavior in darwinian hydrologic models. *Geophysical Research Letters*, *41*(13), 4569–4577. https://doi.org/10.1002/2014GL060509

Wang, D., Wang, G., & Anagnostou, E. N. (2007). Evaluation of canopy interception schemes in land surface models. *Journal of Hydrology*, *347*(3–4), 308–318. https://doi.org/10.1016/j.jhydrol.2007.09.041

Wang, D., Zhao, J., Tang, Y., & Sivapalan, M. (2015). A thermodynamic interpretation of Budyko and L'vovich formulations of annual water balance: Proportionality Hypothesis and maximum entropy production. *Water Resources Research*, *51*(4), 3007–3016. https://doi.org/10.1002/2014WR016857

Wang, L., Good, S. P., & Caylor, K. K. (2014). Global synthesis of vegetation control on evapotranspiration partitioning. *Geophysical Research Letters*, *41*(19), 6753–6757. https://doi.org/10.1002/2014GL061439

Wu, Q., Lane, C. R., Wang, L., Vanderhoof, M. K., Christensen, J. R., & Liu, H. (2019). Efficient delineation of nested depression hierarchy in digital elevation models for hydrological analysis using level-set method. *Journal of the American Water Resources Association*, *55*(2), 354–368. https://doi.org/10.1111/1752-1688.12689

Yu, F., & Harbor, J. M. (2019). The effects of topographic depressions on multiscale overland flow connectivity: A high-resolution spatio-temporal pattern analysis approach based on connectivity statistics. *Hydrological Processes*, *33*(10), 1403–1419. https://doi.org/10.1002/hyp.13409

Zapata-Rios, X., Brooks, P. D., Troch, P. A., McIntosh, J., & Guo, Q. (2016). Influence of terrain aspect on water partitioning, vegetation structure and vegetation greening in high-elevation catchments in northern New Mexico. *Ecohydrology*, *9*(5), 782–795. https://doi.org/10.1002/eco.1674

Zeng, X. (2001). Global vegetation root distribution for land modeling. *Journal of Hydrometeorology*, *2*(5), 525–530. https://doi.org/10.1175/1525-7541(2001)002<0525:gvrdfl>2.0.co;2

Zhou, S., Yu, B., Zhang, Y., Huang, Y., & Wang, G. (2016). Partitioning evapotranspiration based on the concept of underlying water use efficiency. *Water Resources Research*, *52*(2), 1160–1175. https://doi.org/10.1002/2015WR017766